Czech Technical University in Prague
Faculty of Nuclear Sciences and Physical Engineering

Department of Physics

Master's thesis

Study of charge asymmetry in top quark pair production in ATLAS experiment

Bc. Jakub Cúth
2013

Supervisor: RNDr. Roman Lysák, PhD

Work tittle: **Study of charge asymmetry in top quark pair production in ATLAS experiment**

Department: Department of Physics, Faculty of Nuclear Sciences and Physical Engineering

Author: Bc. Jakub Cúth

Branch of study: Nuclear engineering

Kind of project: Master's thesis

Supervisor: RNDr. Roman Lysák, PhD

Abstract: The top quark in proton-proton collisions at centre-of-mass energy 7 TeV at Large Hadron Collider (LHC) has been studied. The data corresponding to integrated luminosity $4.7\,\mathrm{fb}^{-1}$ has been recorded by ATLAS experiment in year 2011. There is predicted slight charge asymmetry in top quark pair production, which at LHC could be observed in the distribution of the difference between absoulute rapidity of the top quark and anti-quark. Because the measurement is performed in the dilepton channel, the lepton charge asymmetry could be studied in the distribution of difference between absolute pseudorapidity of positive and negative leptons. The main goal of this thesis is to study the unfolding of above mentioned distributions from detector to parton level.

Keywords: CERN, Large Hadron Collider, ATLAS experiment, top quark, charge asymmetry, dilepton channel, Bayesian iterative unfolding

Název práce: **Studium nábojové asymetrie v produkci párů top kvarků na experimentu ATLAS**

Katedra: Katedra Fyziky, Fakulta Jaderná fyzikálně Inženýrská

Autor: Bc. Jakub Cúth

Obor: Jaderné inženýrství

Druh práce: Diplomová práce

Vedouci práce: RNDr. Roman Lysák, PhD

Abstrakt: Tato práce studuje produkci párů top kvarků ve srážkách na urychlovači LHC při těžišťové energii 7 TeV. Měření bylo provedeno detektorem ATLAS a naměřená data za rok 2011 odpovídají luminozitě 4.7 fb^{-1}. Je předpovězena nábojová asymetrie v produkci párů top kvarků, která může být na urychlovači LHC pozorována v distribuci rozdílu absolutních hodnot rapidity top kvarku a anti-kvarku. Díky tomu, že měření je prováděno v dvoj-leptonovém kanále, je možné měřit též nábojovou asymetrii leptonů, a to v distribuci rozdílu absolutních hodnot pseudorapidit kladného a záporného leptonu. Hlavním cílem této práce je studium dekonvoluce výše zmíněných distribucí z detektorové úrovně na úroveň partonovou.

Klíčová slova: laboratoř CERN, urychlovač LHC, experiment ATLAS, top kvark, nábojová asymetrie, dvoj-leptonový kanál, Bayesova iterativní dekonvoluce

Prohlášení

Prohlašuji, že jsem svoji diplomovou práci vypracoval samostatně a použil jsem pouze podklady uvedené v přiloženém seznamu.

Nemám žádný důvod proti užití tohoto díla ve smyslu §60 Zákona č. 121/2000 Sb., o právu autorském, o právech souvisejících s právem autorským a o změně některých zákonů (autorský zákon).

Declaration

Here I declare that I wrote my master thesis independently and exclusively with the use of cited resources.

I agree with the usage of this thesis in accordance with the Act 121/2000 (Copyright Act).

V Praze dne ______________________ ____________________________

Bc. Jakub Cúth

Acknowledgement

First of all, I would like to express my gratitude to my supervisor Roman Lysák for the patience and guidance during my master's research. Also I would like to thank all my colleagues from Institute of Physics in Prague and Košice for assistance.

Contents

Contents **2**

Introduction **3**

1 Top quark physics **5**
- 1.1 Standard Model . . . 5
  - 1.1.1 Elementary particles . . . 6
  - 1.1.2 Quantum field theories . . . 9
- 1.2 Top quark production mechanism . . . 12
- 1.3 Decay modes of top-quark . . . 13
- 1.4 Charge asymmetry in top-quark pair production . . . 14

2 The ATLAS experiment **19**
- 2.1 ATLAS Detector . . . 20
  - 2.1.1 Inner detector . . . 23
  - 2.1.2 Calorimeters . . . 24
  - 2.1.3 Muon Chambers . . . 26
- 2.2 ATLAS trigger system and data acquisition . . . 28
  - 2.2.1 Level-1 . . . 28
  - 2.2.2 High level trigger . . . 29

3 Computing software **31**
- 3.1 Official ATLAS software framework . . . 31
  - 3.1.1 Athena framework . . . 31
  - 3.1.2 Event Data Model . . . 33
- 3.2 Distributive computing on GRID . . . 36
- 3.3 ROOT . . . 38
- 3.4 Data preparation . . . 40

4 Measurement of charge asymmetry **43**
- 4.1 Event selection . . . 43
- 4.2 Modeling of signal and background . . . 44

4.3 Kinematic reconstruction of $t\bar{t}$ system 46

5 Unfolding studies **49**

5.1 General notes 49

5.2 Deconvolution methods 51

5.2.1 Bin-by-bin method 51

5.2.2 Response matrix inversion 52

5.2.3 Singular value decomposition 52

5.2.4 Iterative D'Agostini method 53

5.2.5 Comparison of the unfolding methods 54

5.3 Bayesian method optimization 55

5.3.1 Asymmetry and number of iterations 56

5.3.2 Pseudo-experiments 57

5.4 Corrections and uncertainties 65

Conclusions **67**

A Response matrices **69**

Bibliography **74**

Introduction

If we want to know, how the machine works, we have to take it apart to the basic pieces and get to know how one part affects each other. The situation is similar in case of understanding the Universe. The deepest fundamental knowledge about the World is that all matter consists of small particles, which interact with each other by four fundamental forces: electromagnetic, weak, strong and gravitational. The most successful theory describing the elementary particles and interactions is the Standard Model. However, the Standard Model (SM) can not explain some observed phenomena and the search for "new physics" beyond the SM is performed by high energy physics experiments.

One of the fundamental particles is the top quark. Since its first observation at proton–anti-proton collider Tevatron in 1995 it is mesmerizing research object, which is very useful for testing of the Standard Model predictions. As the heaviest elementary particle with the invariant mass of 173.5 GeV it can be produced in high energetic collisions only. Such collisions are provided by Large Hadron Collider (LHC) – the most powerful particle accelerator in the World situated on Franco-Swiss border near Geneva in the CERN laboratory. In this work, we study the top quark recorded by ATLAS experiment – the biggest of four main LHC experiments. During the year 2011 the ATLAS detector has recorded collisions at centrer-of-mass energy of 7 TeV corresponding to integrated luminosity of $4.7\,\mathrm{fb}^{-1}$. The Standard Model predicts about 780 000 of top quark pairs produced in such collisions. This makes the LHC a top quark factory and the ideal environment for detailed studies of top quark properties.

Our analysis is focused on charge asymmetry of top quark pair production. It is predicted by Standard Model that top quarks are not produced uniformly in space and this spatial distribution is different for top quarks and for top anti-quarks. However, the recent measurements at Tevatron point to higher charge asymmetry than it is predicted by the Standard Model. Therefore the measurements at LHC experiments are anticipated. Thanks to the fact that the analysis has been performed in dilepton final state channel, it is giving us the opportunity to measure also the lepton charge asymmetry, which is correlated with top charge asymmetry.

In order to compare the distributions from different experiments and theories, the measured distribution bias originating from detector acceptance and measurement process must be removed. This procedure is called unfolding and the main goal of this thesis is to find the best way how to unfold the distributions where the charge asymmetry is observed.

After this introduction, there is brief description of the Standard Model and top quark physics in Chap. 1. Next chapters contain the description of ATLAS detection system (Chap. 2) and the software framework (Chap. 3). The criteria to select the $t\bar{t}$ events and reconstruction algorithm is summarized in Chap. 4. Finally, the unfolding studies are described in Chap. 5 and the summary of the results can be found in conclusion at the end of this work.

Chapter 1

Top quark physics

Current most successful theory of particle physics is called Standard Model (SM). This theory will be briefly described in this chapter inspired by [1]. Firstly, the particles and interactions of Standard Model are presented. Secondly, there is description of top quark production and decay. Finally, we will describe origin and of the top charge asymmetry in $t\bar{t}$ events.

1.1 Standard Model

The discovery of electron by J.J. Thomson in 1897 [2] could be considered as beginning of modern particle physics. As it has been later appeared, the electron is elementary particle carrying smallest possible value of free electric charge. There were coming out new and new particles after discovery of atom and its internal structure. Due to big boom of number of particles in the 60's and 70's – the golden era of particle physics – physicists felt the necessity of research and finding among them the truly elementary particles without internal structure.

The particle physics uses different system of units classical Newtonian physics. The natural unit system is based on postulation $\hbar = c = 1$[1]. As natural unit of charge is used the absolute value of electric charge |e| of electron. The natural unit of energy is electronvolt eV, which corresponds to energy of particle with charge 1 |e| accelerated in electric field 1 V. Because this is a small unit, the standard multiples are used usually (keV, MeV, GeV, TeV). Also kinematic quantities have units derived from energy. For example momentum $E = p \cdot c \Rightarrow [p] = \mathrm{MeV/c}$ or mass $E = m \cdot c^2 \Rightarrow [m] = \mathrm{MeV/c^2}$.

Since c and $\hbar$ are equal to one, it is common not to write these symbols. Consequently the mass, energy and momentum will have the "same" quantity (e.g. MeV) and lot of equations will have more economical form. On the other hand, it is needed to think about the correct notation.

Relativistic physics (near-speed-of-light physics) treats time and spatial coordinations equally. Therefore it is handy to use four-vector notation. The four-vectors will be symbolized by lower case letters and their elements will be denoted by lower index for covariant and upper index for contravariant form. The zeroth element represents time (or energy) component and next three components represents classical spatial (or momentum) three-vector. Classical three component

---

[1] Here and after $\hbar$ is reduced Plank constant and c is speed of light in vacuum

vectors will be symbolized by arrow above character.

$$x = (x_0, x_1, x_2, x_3) = (c \cdot t, \vec{x}) \tag{1.1a}$$

$$p = (p_0, p_1, p_2, p_3) = (\frac{E}{c}, \vec{p}) \tag{1.1b}$$

The particle physics is usually studied by two particle reactions like collisions or fixed target experiments. The physical invariants are always welcome, therefore Lorentz-invariant Mandelstam variables are defined in two body reactions as

$$s = (p_1 + p_2)^2 = (p_3 + p_4)^2 \tag{1.2a}$$

$$t = (p_1 - p_3)^2 = (p_2 - p_4)^2 \tag{1.2b}$$

$$u = (p_1 - p_4)^2 = (p_2 - p_3)^2 \tag{1.2c}$$

$$s + t + u = m_1^2 + m_2^2 + m_3^2 + m_4^2 \ , \tag{1.2d}$$

where p is momentum four-vector, m is invariant mass. The indices 1 and 2 represents input particles and indices 3 and 4 represents output particles. More collision-related kinematic quantities could be found in section 2.1.

1.1.1 Elementary particles

The best way how to describe particles is to group them according to their physical properties – quantum numbers. Beside the physical quantities as mass and charge, which are well known and does not need to be introduced, there are some of properties, like spin, which has no analogical observable in classical physics.

The spin has no equivalent in classical physics. The first postulation of spin has been made by W. Pauli in 1925 [3] as a property of electrons in atom shell having only two values $\pm 1/2\hbar$. Owing to arithmetic operations, the spin is usually denoted as intrinsic angular momentum, even though there is no evidence of an intrinsic-rotation of elementary particles.

Due to explanation of atom orbital build-up, an exclusion principle has been purposed by Pauli saying that no two electrons could be in state with the same quantum numbers. Latter it has appeared that spin is intrinsic property of all particles, however not every particle fulfils Pauli exclusion principle. As a result, the particles could be divided into two groups:

Bosons are particles with whole integral spin ($S = 0, 1, 2, \dots$). They follow Bose-Einstein statistics and do not fulfil Pauli exclusion principle. The wave function of spin-0 particles ϕ is transformed as scalars in Lorentz-transformations. The equation of motion describing the free spin 0 particle is called Klein-Gordon equation

$$(\partial_\mu \partial^\mu - m^2)\phi = 0 \ , \tag{1.3}$$

where $\partial_\mu = (\partial_t, \partial_x, \partial_y, \partial_z)$ and $\partial^\mu = (\partial_t, -\partial_x, -\partial_y, -\partial_z)$ are four-derivations.

Fermions , as particles with half-integral spin ($S = 1/2, 3/2, 5/2, \dots$), fulfil Pauli exclusion principle and multi-fermion system is described by Fermi-Dirac statistics. The spin-$\frac{1}{2}$ fields are usually represented by spinors ψ and the free propagation half-spin field could be derived from Dirac equation

$$(\not{\partial} + m)\psi = 0 \ , \tag{1.4}$$

where $\not{\partial} = \gamma_\mu \partial^\mu$ is four-derivation in Feynman slash notation.

One of the consequences of the Dirac equation is the fact it has two solutions with opposite sign of electric charge. Dirac explained this fact by the idea of the vacuum as infinite sea filled with electrons. When the electron has been removed from the sea, as a result there appears empty space in sea of the electrons. This empty place in electron-filled sea could be observed as anti-particle – positron – having the same physical properties as electron but the opposite sign of charge and magnetic momentum.

It is well-known today that all fermions have their anti-partner and the same situation is among bosons, however some of bosons are anti-particles to themselves.

Let one constructs a multi-particle wave function ψ. If inside this wave function one interchanges two identical fermions the multi-particle wave function changes the sign: $\psi \to -\psi$. While in case of identical-bosons-exchange the sign of function is the same. This is called spin-statistic theorem and as a result one can say, that the fermions are sensitive to their type. The quantum number of “kind” of fermions is called flavour.

The electron is one of the twelve elementary fermions of Standard Model, which all matter is consisting of. By definition the fermions, which are not taking part in strong interactions, are called leptons. There are six leptons ℓ: electron e, muon μ, tauon τ and their neutrinos ν_e, ν_μ, ν_τ. The electrons, muons and tauons are massive particles with electric charge $-1|e|$ and on the other hand, the neutrinos interact only weakly, have tiny mass[2] and are electrically neutral.

The other six elementary fermions are called quarks. The quarks q have electric charge $+2/3|e|$ (for up u, charm c, top t) or $-1/3|e|$ (for down d, strange s, bottom b). The quarks have never been observed as free particles. This phenomena is called quark confinement and it can be explained by running coupling constant of strong interaction, which is increasing with the distance.

The quarks are observed within bound state of two or three quarks (anti-quarks). Such a state is called hadron. The strong interaction bound quarks together as “strongly” as if one tries to “detach”

---

[2] According to Standard Model the neutrinos are massless however, there is evidence of neutrino non-zero mass. Moreover the mass of neutrinos is so small it could be considered as zero in calculations.

a quark from hadron, it will need as much energy as it is needed to create another quark pair and thereby to create new hadron.

Owing to large number of hadrons, the classification based on their internal structure has been presented even before the existence of quark has been known. Latter when the Quark Model has been developed, some of properties has been explained and the calculations with hadrons has been simplified. As Quark Model predicts the hadrons are divided into two groups:

Mesons are bosons, which are consisting of one quark and one anti-quark (from Greek $\mu\varepsilon\sigma o\varsigma$, mésos, "middle" or "intermediate"). If one takes as constituent quarks u, d, s and c, the 16-plet coul be created based on decomposition

$$\mathbf{4} \otimes \bar{\mathbf{4}} = \mathbf{15} \oplus \mathbf{1} \tag{1.5}$$

According to the spin addition of the constituent quarks there are pseudoscalars mesons (spin-0) or vector mesons (spin-$\frac{1}{2}$). There are also mesons containing b-quark. Such hadrons are interesting due to their rarity and long lifetime and the B-physics is discipline engaged in b-hadrons.

Baryons are fermions and consists of three quarks or three anti-quarks (form Greek $\beta\alpha\rho\upsilon\varsigma$, barús, "heavy"). The "ordinary" baryons are formed by u, d, s quarks and the group could be written as

$$\mathbf{3} \otimes \mathbf{3} \otimes \mathbf{3} = \mathbf{10}_S \oplus \mathbf{8}_M \oplus \mathbf{8}_M \oplus \mathbf{1}_A \tag{1.6}$$

where the indexes "S", "M" and "A" mean symmetric, mixed-symmetry or antisymmetric, respectively. The baryonic multiplets could be extended to $SU(4)$. Consequently the possible combinations of u, d s and c quarks could be reduce to two 20-plets, one with $SU(3)$ octet and one with $SU(3)$ decuplet. If the b quark is added as constituent, the group will be $SU(5)$. Also the anti-baryons would form the same multiplets but with anti-quarks as constituents.

Quarks, as fermions, have to follow Fermi exclusion principle, which says that there are no two fermions which have identical all quantum numbers. However, there are baryons (e.g. Δ^{++}), which have three quarks of the same flavour (u), and the same spin orientation ($\uparrow\uparrow\uparrow$). Consequently the quarks must have another degree of freedom, which has not been observed outside the hadrons.

This discrete degree of freedom has been named "color", because of analogous arithmetic operations with color addition. Each quarks carries a "color charge" – red r, green g or blue b; and each anti-quark carries "anti-color charge" – anti-red $\bar{r}$, anti-green $\bar{g}$ or anti-blue $\bar{b}$. When quarks form a hadron the "color" is canceled out (white "color" w) e.g. hadrons $r + g + b = w$, $\bar{r} + \bar{g} + \bar{b} = w$ or mesons $r + \bar{r} = w$.

The strong nuclear force (or "color" exchange) is intermediated by bosons gluons (from English *glue*). The gluons are massless, spin 1, electrically neutral particles which are responsible for quark confinement. The quantum field theory describing the strong interaction is called Quantum Chromodynamics (QCD) and it will be described later (subsection 1.1.2).

To sum it up, the Standard Model particles are elementary constituent fermions and interaction bosons. Fermions are grouped into three families and each family consists of two quarks and two leptons. Each next family particles are have higher mass and shorter lifetime.

Three fundamental forces are intermediated by spin-1 bosons. The gluons G are strong interaction bosons, the photon γ intermediates electromagnetic force, and intermediation bosons of weak interaction are $W^{\pm}$ and Z^0.

All but one particles has already been observed and experimentally confirmed. The last piece of Standard Model is Higgs boson. It is predicted that all particles interact with Higgs boson and through spontaneous symmetry breaking is Higgs boson responsible for masses of all Standard Model particles. The observation of new boson has been announced by ATLAS and CMS experiments at LHC in July 2012. This boson has been discovered in predicted Higgs decay channels $H \to \gamma\gamma$ and $H \to 4\ell$. The mass of new boson has been estimated $\sim 126\,\mathrm{GeV}$.

In table 1.1 are summarized basic properties of fundamental particles of Standard Model.

1.1.2 Quantum field theories

The study of matter on particle scale ($\sim 10^{-15}\,\mathrm{m}$) reveal effects and phenomenons, which are not observable on ordinary-life scales. One of the first effect is neglecting of gravitational interactions, because of gravitational coupling constant is much smaller comparing to other interactions.

Furthermore lot of physical observables have only discrete spectrum. The mathematical description of this kind of system had to be developed – the quantum physics. The correspondence principle has been complied from the very beginning of developing the quantum theory. It says that if one extends the quantum physics relations to classical scale of length and energy, the laws of classical physics have to be obtained. Also the formalisms, which we know from classical theoretical physics is widely used in quantum theory, i.e. Lagrangian, Hamiltonian, equations of motion etc.

Because of existence of wave-particle duality, particles in quantum physics are described by wave-function. The wave-function is element of Hilbert space of possible states of the particle. Furthermore the creation and annihilation of particles has been observed in nature, therefore the Hilbert space is a sum of Hilbert subspaces each representing one multiplicity of the particle.

The wave-function is highly abstract term and sometimes it is difficult to present its physical interpretation. Typically the squared magnitude of wave function represents the probability of particle state. This is consistent with probabilistic interpretation of quantum physics and Heisenberg uncertainty principle [5].

Generally in physics, the successful description of system is the one, which also after evolution in time is still consistent with observations. Time evolution is mathematically expressed by Hamiltonian. However, more efficient way how to set up this formalism is trough minimum action principle and construction of Lagrangian. In addition, the transition from Lagrangian to Hamiltonian is equivalent to transition between canonical variables $p \to q$, where p and q are generalized momentum and coordinates respectively [6].

		fermion family		
spin	**charge**	I	II	III
1/2	$+\frac{2}{3}$	u 2.3 MeV	c 1.275 GeV	t 173.5 GeV
	$-\frac{1}{3}$	d 4.8 MeV	s 95 MeV	b 4.18 GeV
	-1	e 0.511 MeV	μ 105.66 MeV	τ 1.77 GeV
	0	ν_e < 225 eV	ν_μ < 0.19 keV	ν_τ < 18.2 MeV
			interaction	
1	0	γ 0	electromagnetic	
	0	Z 91.187 GeV	weak	
	±1	W 80.385 GeV		
	0	G 0	strong	
0	0	H ???	SM Higgs field	

Table 1.1: Elementary particles of Standard Model. The values under particle symbol is the invariant mass and all values are from [4]. For more description see text.

Also in the quantum field theory, the basic tool helping with Lagrangian construction is Noether theorem [7], which says, that each conservation law corresponds to symmetry under group[3] of continuous transformations. It means that each observed conserved quantity in the system constrains the Lagrangian.

$$\begin{array}{ccccc} SU_c(3) & \times & SU_L(2) & \times & U_Y(1) \\ \downarrow & & \downarrow & & \downarrow \\ G^{\alpha}_{\mu} & & W^{a}_{\mu} & & B_{\mu} \\ \alpha = 1, \cdots, 8 & & a = 1, \cdots, 3 & & \end{array} \tag{1.7}$$

The Standard Model gauge symmetry is described by product of groups Eq. 1.7. The three W^a_μ are spin-1 generators of $SU_L(2)$ group, where subscript "L" meant that only left-handed fermions are carriers of this quantum number. The B_μ is the gauge boson of $U_Y(1)$ group, where the "Y" stands for weak hypercharge which is defined as $Q = T_3 + Y$, where Q is electric charge and T_3 is projection of third component of the isospin.

These four spin-1 particles W^a_μ and B_μ are related to physical bosons $W^\pm$, Z^0 intermediating weak force and photon γ familiar from Quantum Electrodynamics (QED) – quantum field theory of electromagnetic interaction.

To conclude the $SU_L(2) \times U_Y(1)$ is symmetry associated to electroweak theory (EW) – quantum field theory unifying the electromagnetic and weak interactions. Because all fermions have non-zero weak hypercharge they can interact weakly, and all charged fermions interact also electromagnetically.

If the Lagrangian is based only on $SU_L(2) \times U_Y(1)$ symmetry all particles will be massless and this is in contradiction with the observations. Therefore, something must be added to our theory, which will provide masses to all particles. The simplest method, which preserves SM symmetries, is addition of Higgs field – the scalar doublet with the potential minimized at none-zero-field value. This procedure of "creating" the particle masses is called spontaneous symmetry breaking.

The generators of $SU_c(3)$ group represents the octet of spin-1 particles – gluons G^α_μ. The subscript "c" stands for color (understood as the quantum number), which means each particle carrying the color couples to gluons. The gluons are intermediate bosons of strong force and the quantum field theory describing this interaction is called Quantum Chromodynamics (QCD).

Although the spontaneous symmetry breaking affects all fermion masses, the quarks – carriers of color charge – are not observed as free particles, but they are bound inside hadrons. Therefore is hard to measure quark invariant mass.

Therefore the discovery of quarks has not been straightforward and there was many different theories, which were giving better or worse predictions. For instance the parton model is the one of the best approximations of internal kinematic structure of hadrons and it is still in use. The idea is

---

[3] The description of group theory suitable for physical applications can be found in [8].

that the particles (named partons) inside a hadrons are carrying the fraction of the whole hadron momentum.

The measurements of lepton–nucleon deep inelastic scattering (DIS) are indicating that inside the nucleons are three massive charged particles associated to quarks and massless neutral (gluon) field. The partons density function (PDF) is the probability of finding the quark or gluon with momentum[4] $x\vec{p}$ in nucleon with momentum $\vec{p}$.

The Quark Model is in coincidence with Parton Model for valence constituent partons (u and d). However there is non-zero probability of finding also heavier quarks (or anti-quarks) inside nucleon. Those non-valence quarks are called sea quarks. As a result the contribution from both valence and sea components are taken into account in the calculations of proton-proton collision processes.

1.2 Top quark production mechanism

The top quark is an engrossing research object and instrument for testing of Quantum Chromodynamics predictions. As has been mentioned above (see 1.1.1) top quark is strong-interacting fermion with spin $S = 1/2$, electric charge $Q = +2/3|e|$ and mass $m_t = (173.5 \pm 0.1)$ GeV [4].

The top quark is much heavier than has been expected. According to last experimental results it is heaviest elementary particle.As the last discovered elementary fermion, the top quark has been observed for first time at $p\bar{p}$-collider Tevatron in 1995 by two detectors CDF [9] and D0 [10]. It was almost 20 years after discovery of b-quark, lighter quark of the third generation, which has been indirect proof of top existence.

Usually the heavy quarks have been discovered by their hadronic bound states like quarkonia $J/\psi = c\bar{c}$ or $\Upsilon = b\bar{b}$. While the top quark has been detected by its direct decay products (see section 1.3). Due to top short lifetime $\tau = 3.3 \cdot 10^{-25}$ s (according to top full decay width $\Gamma = 2$ GeV [4]), top does not manage to create bound state with any other quark.

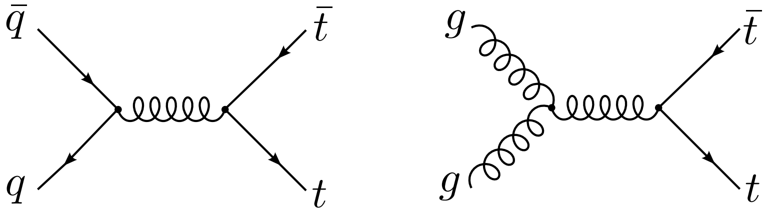

(a) Quark anihilation.

(b) Gluon fusion.

Figure 1.1: The Feynman diagrams of leading order $t\bar{t}$ production.

Because the quantum number – flavour – is conserved in QCD interactions, only top quark pair production is allowed in QCD. The simplest production mechanism at leading-order (LO) of

---

[4] The fraction x is real number $x \in (0; 1)$.

perturbative Quantum Chromodynamics (pQCD) are showed at Fig. 1.1.

The dominant LO production mechanism at LHC collision energy $\sqrt{s} = 7\,\mathrm{TeV}$ is gluon–gluon fusion (Fig. 1.1b) . With higher energies the next terms of pQCD are more relevant for $t\bar{t}$ production. The theoretical cross-section of $t\bar{t}$ production $\sigma_{t\bar{t}} = 166.78^{+16.48}_{-17.76}\,\mathrm{pb}$ has been calculated by program HATHOR [11] with top mass 172.5 GeV and input parameters matching condition of pp-collision at LHC in 2011.

Some of NLO diagrams and contribution to top charge asymmetry is described later in section 1.4.

The electroweak theory allows flavour changing in charged currents and consequently allows to produce single top quark. There are three main production processes s-channel Drell-Yan, t-channel Wb fusion and associated Wt production (see Fig. 1.2). The theoretical cross-section of single top production at $\sqrt{s} = 7\,\mathrm{TeV}$ is $\sim 66\,\mathrm{pb}$ predicted by SM [12]. In our case single-top production has been taken into account only as a background.

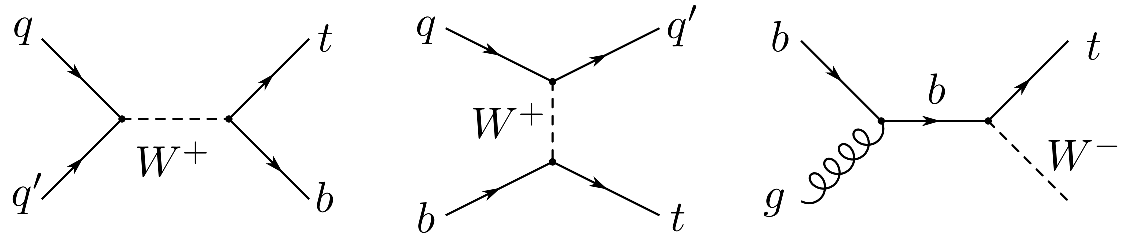

(a) s-channel. (b) t-channel. (c) Associated Wt production.

Figure 1.2: The Feynman diagrams of single top production.

1.3 Decay modes of top-quark

Due to absenting neutral flavour changing current, the dominant decay mode of top quark is induced by weak charged currents, [13]

$$\Gamma(t \to W^+q) = \frac{|V_{tq}|^2 m_t^3}{16\pi v^2}(1 - \frac{m_W^2}{m_t^2})^2(1 + 2\frac{m_W^2}{m_t^2})\left[1 - \frac{2\alpha_s}{2\pi}\left(\frac{2\pi^2}{3} - \frac{5}{2}\right)\right] , \tag{1.8}$$

and since $|V_{tb}| \gg |V_{td}|, \ |V_{tu}|$ the preferred top decay mode is

$$t \to Wb \tag{1.9}$$

In short the top decay channels depends on the decay products of W. Generally the W-boson decays into two fermions – leptons or quarks. The decay into quarks is called hadronic, because as has been mentioned before the quarks are bounded inside hadrons right after W decay. The products of leptonic decay of W are lepton and its anti-neutrino or vice versa.

Decay mode	Calculated	Measured
$e^+\nu_e$	11.1%	(10.75 ± 0.13)%
$\mu^+\nu_\mu$	11.1%	(10.57 ± 0.15)%
$\tau^+\nu_\tau$	11.1%	(11.25 ± 0.20)%
hadrons	66.7%	(67.60 ± 0.27)%

Table 1.2: Branching ratios of W^+ decay modes. The measured values are from [4] and for calculated values see the text.

The branching ratios between decay channels could be calculated simply from particular decay widths. The total decay width of W could be derived from EW as

$$\Gamma_{\text{tot}} = \Gamma(W^+ \to e^+\nu_e)\left[3 + 3\sum_{n=1}^{2}\sum_{m=1}^{3}|V_{nm}|^2\right] , \tag{1.10}$$

where the first term in square brackets "3" represents the three families of leptons. The second term in square brackets is multiplied by 3 due to three possible colors of quarks. The first sum runs over first two families, because the W mass is insufficient to produce top quark. The $|V_{nm}|$ represents element of CKM matrix and by using its unitarity we obtain

$$\sum_{n=1}^{2}\sum_{m=1}^{3}|V_{nm}|^2 = \sum_{n=1}^{2}[VV^\dagger]_{nn} = 2 . \tag{1.11}$$

Now it is possible to calculate branching ratios $R_i = \frac{\Gamma_i}{\Gamma_{\text{tot}}}$ even without the knowledge of the value $\Gamma(W^+ \to e^+\nu_e)$. The calculated and measured values are summarized in table 1.2.

As a consequence of the facts mentioned above the possible decay channels (see Fig. 1.3) of the $t\bar{t}$ are:

fully hadronic Both W bosons decay into quark pairs. This channel is characterised by four light jets and two b-jets.

lepton+jet One W decays into leptons and other decays into quark pair. This events contain isolated lepton (electron or muon), missing transverse momentum (from escaped neutrino), two light jets and two b-jets.

dilepton Both W bosons decay into lepton pairs. Two isolated leptons (electrons or muons), missing transverse momentum (from two neutrinos) and two b-jets are the specific products of this channel.

1.4 Charge asymmetry in top-quark pair production

The Quantum Chromodynamics production of top–anti-top quark pair is asymmetric under charge conjugation [14]. In brief there is higher probability of forward top quark than anti-quark in parton

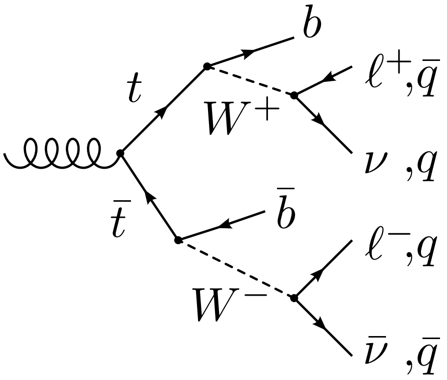

Figure 1.3: Schematic $t\bar{t}$ decay chain.

frame. The dominant leading order production mechanism at LHC collision energy $\sqrt{s} = 7\,\text{TeV}$ is gluon–gluon fusion Fig. 1.1b. However this three gluon coupling is fully symmetric and therefore it will suppress the overall asymmetry. The source of asymmetry is from the quark annihilation Fig. 1.1a interferences. The first is the interference of final and initial state radiation of gluon and the second is the interference of the Box and Born diagrams (see fig 1.4).

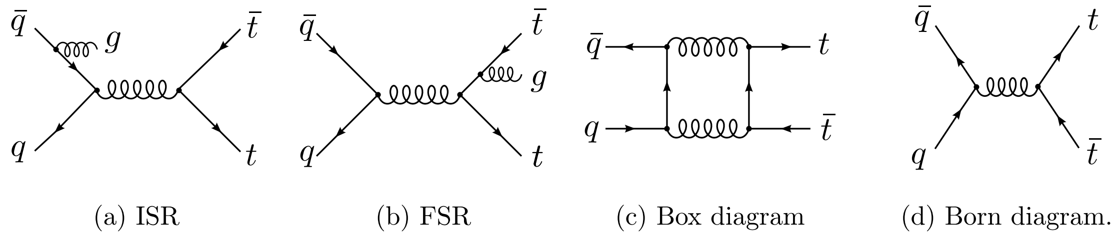

(a) ISR (b) FSR (c) Box diagram (d) Born diagram.

Figure 1.4: The Feynman diagrams of LO interference-induced asymmetry, ISR–FSR on sub-figures a) and b), respectively and Box–Born on sub-figures c) and d), respectively.

Furthermore there is higher contribution of NLO terms on LHC collision energy than at Tevatron. Except the gluon–gluon fusion all NLO diagrams are asymmetric under charge conjugation (see fig. 1.5). Because the interferences are in higher order of α_s the LO generators can not predict the top charge asymmetry. Generally, the asymmetry rises with overall rapidity of $t\bar{t}$ system and also higher asymmetry is predicted at higher invariant masses of $t\bar{t}$ system. Therefore it is suitable to look at asymmetry with respect to the mentioned kinematic variables.

The asymmetry can be measured by rapidity distribution (defined in Eq. 2.3) of the top quark and anti-quark. There are several possible definitions of asymmetry. Due to charge asymmetry on $p\bar{p}$ colliders like Tevatron the forward-backward asymmetry could be observed. This means that top quark is preferentially produced in the direction of incoming proton and top anti-quark in direction of anti-proton (Fig. 1.6a). The forward-backward asymmetry could be defined as

$$A_{FB} = \frac{N_F - N_B}{N_F + N_B} \ , \tag{1.12}$$

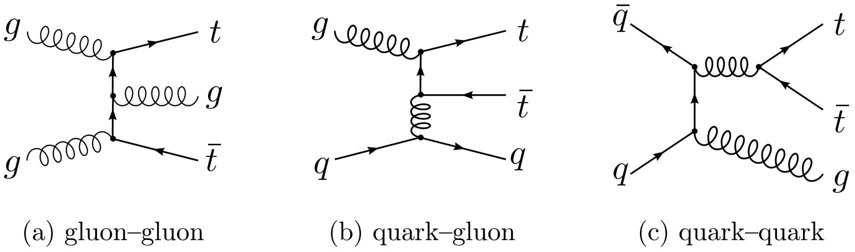

(a) gluon–gluon (b) quark–gluon (c) quark–quark

Figure 1.5: Examples of next-to-leading order $t\bar{t}$ production Feynman diagrams.

where N_F is number of forward events when $y_t - y_{\bar{t}} > 0$ and N_B is number of backward events when $y_t - y_{\bar{t}} < 0$. The predicted value of A_{FB} is $\sim 7.0\%$ at Tevatron collision energy [15].

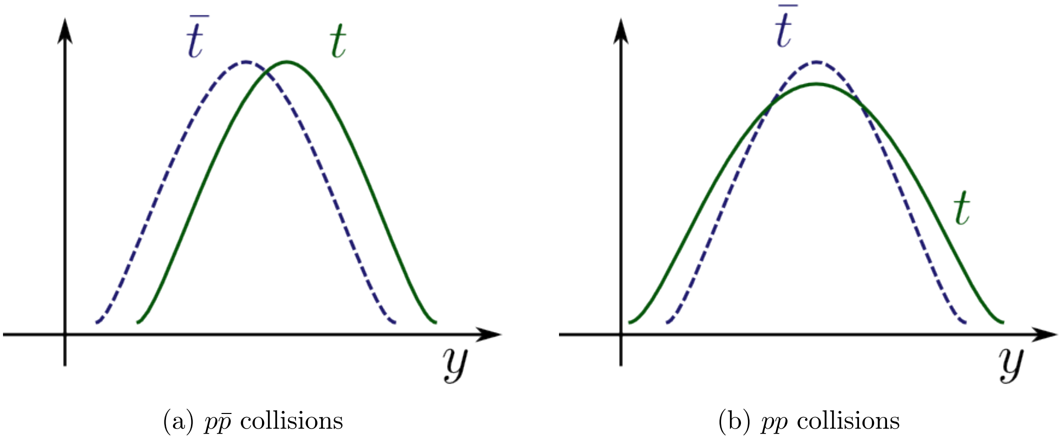

(a) $p\bar{p}$ collisions (b) pp collisions

Figure 1.6: Illustrative rapidity distribution of top quark (green solid line) and anti-quark (blue dashed line) expected in pp and $p\bar{p}$ collisions.

The forward-backward asymmetry vanishes at LHC due to symmetric pp collisions. However the slight asymmetry could be observed in suitable chosen distribution. The example of such a distribution is difference between absolute values of top quark and anti-quark rapidities

$$\Delta|y_{t\bar{t}}| \equiv |y_t| - |y_{\bar{t}}| \,. \tag{1.13}$$

According to PDF the quarks inside the protons cary higher momentum fraction than anti-quarks. As result of this and charge asymmetry at parton level, the top quarks will be produced with higher absolute value of rapidity than anti-quarks (Fig. 1.6b). The variable $\Delta|y_{t\bar{t}}|$ is positive if the top quark is “more forward” than the top anti-quark and vice versa. Consequently, the top charge asymmetry could be defined as

$$A_C^{t\bar{t}} = \frac{N(\Delta|y_{t\bar{t}}| > 0) - N(\Delta|y_{t\bar{t}}| < 0)}{N(\Delta|y_{t\bar{t}}| > 0) + N(\Delta|y_{t\bar{t}}| < 0)} \tag{1.14}$$

where N means number of events fulfilling the condition in brackets. The theoretical value of charge asymmetry $A_C^{t\bar{t}} = 0.006 \pm 0.002$ at the LHC has been estimated by MC@NLO generator (described in Sec. 4.2). Because we perform analysis in di-lepton channel also lepton charge asymmetry could be defined

$$A_C^{\ell^+\ell^-} = \frac{N(\Delta|\eta_{\ell^+\ell^-}| > 0) - N(\Delta|\eta_{\ell^+\ell^-}| < 0)}{N(\Delta|\eta_{\ell^+\ell^-}| > 0) + N(\Delta|\eta_{\ell^+\ell^-}| < 0)} \tag{1.15}$$

where N is again number of events fulfilling the condition in bracket and $\Delta|\eta_{\ell^+\ell^-}| \equiv |\eta_{\ell^+}| - |\eta_{\ell^-}|$. The lepton charge asymmetry at the LHC is predicted to be 0.004 ± 0.001 (according to MC@NLO generator).

The results of top forward-backward asymmetry measurement from Tevatron detectors (CDF [16] and D0 [17]) point at higher asymmetry than predicted by Standard Model in some kinematic regions with $2 - 3\sigma$ significance. The measured forward-backward asymmetry is correlated with charge asymmetry. Therefore measurement of charge asymmetry at LHC experiments is important to confirm the deviation of from the SM observed at Tevatron.

The higher charge asymmetry could be induced by physics beyond the Standard Model. For example existence of colored heavy neutral gauge bosons called axigluons could increase the top charge asymmetry with respect to the axigluon mass m_A. The beyond SM theories extend QCD symmetry to $SU_L(3) \times SU_R(3)$ at high energies. The octet of massive generators interact with quarks as axial vectors, therefore the name axigluons. This model has been used for testing the unfolding performance in Chap. 5.

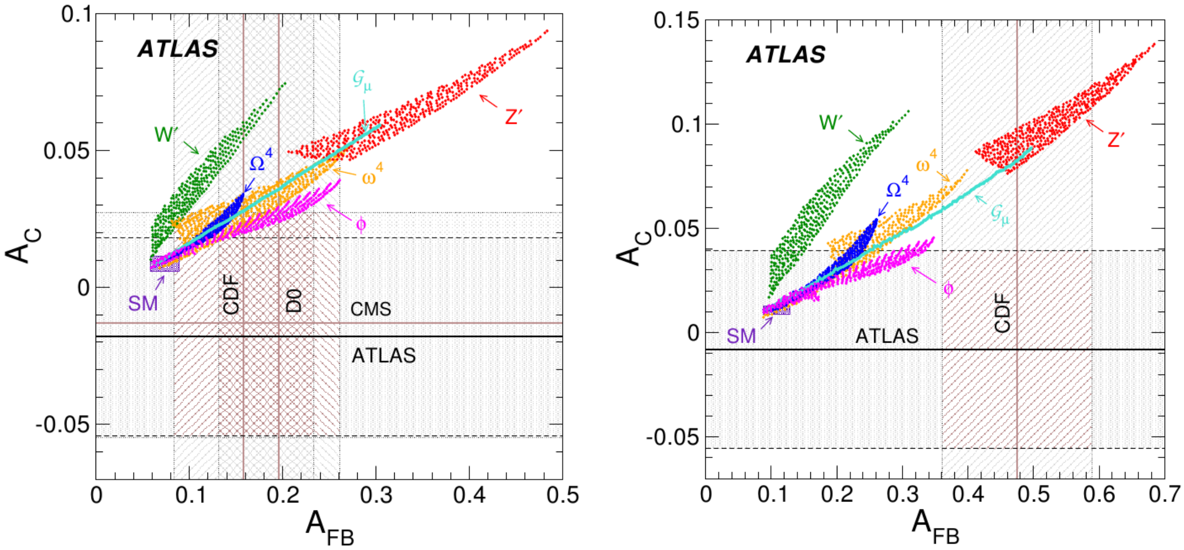

(a) Inclusive asymmetry

(b) $m_{t\bar{t}} > 450\,\mathrm{GeV}$

Figure 1.7: Summary of models beyond the SM with measurements at LHC (A_C) and Tevatron (A_{FB}). Figure from [18]. For more description see the text.

The summary of possible beyond the Standard Model physics contributing to top charge asymmetry could bee seen in Fig. 1.7, where Fig. 1.7a shows the inclusive measured asymmetries and on Fig. 1.7b are plotted asymmetries measured in $m_{t\bar{t}} > 450\,\mathrm{GeV}$ mass region.

On these figures could be found models: flavour changing Z' boson (red area), scalar iso-doublet ϕ (pink area), W' boson (green area) , axigluon $\mathcal{G}_\mu$ (cyan line), scalar color-triplet ω^4 (orange area), scalar color-sextet Ω^4 (blue area) and the Standard Model (violet square).

Chapter 2

The ATLAS experiment

The data, which has been analysed in this thesis, were recorded by the ATLAS experiment [19] (ATLAS is acronym for **A** **T**horoidal **L**HC **A**pparatu**S**). In this chapter we will describe the detection assembly, inspired by [20].

The ATLAS experiment is one of four main experiments at the Large Hadron Collider (LHC) in European Organization for Nuclear Research (CERN from French *Conseil Européen pour la Recherche Nucléaire*) [21]. The CERN laboratory was founded in 1954 to join European institutions involved in nuclear and particle physics. There original number of 12 founding European states is nowadays enlarge to 20 European member states plus many other cooperating states all over the World.

The first accelerator in CERN, 600 MeV Synchrocyclotron (SC) was built in 1957 and in 33 years of service has been primary focused on nuclear physics. Today in CERN there is big accelerator complex on and under ground level and at the very end of the complex there is the biggest and the most powerful synchrotron in the World – Large Hadron Collider. Two beams of protons (or lead ions) inside the collider are accelerated in opposite directions almost to the speed of light and circulate about 100 m under ground on the Franco-Swiss border.

There are four collision point at LHC and around these interaction points the sophisticated detection devices are build: the ATLAS and the CMS are general purpose detectors, the ALICE is focused on heavy-ion collision physics and LHCb studies bottom quark physics.

The protons origin from bottle of hydrogen gas, which is ionized in device called duoplasmatron and protons are filled into first stage of acceleration complex – linear accelerator LINAC2 (see Fig. 2.1). Afterwards protons with energy 50 MeV travel through assembly of accelerators. The next stage is Proton Synchrotron Booster (PSB), where the protons are accelerated to the 1.4 GeV. After that the beams of protons are injected to Proton Synchrotron (25 GeV) followed by Super Proton Synchrotron (SPS, 450 GeV). The last filling, from SPS to LHC, takes about 5 min and the final acceleration energy in LHC ring is 3.5 TeV per beam. The ramping lasts about 20 minutes [23]. The energy of proton beam has been increased to 4 GeV in year 2012. After three-year technical stop, which is planned at the beginning of year 2013, the center-of-mass energy of collision at LHC will be increased to $\sqrt{s} = 14\,\mathrm{TeV}$.

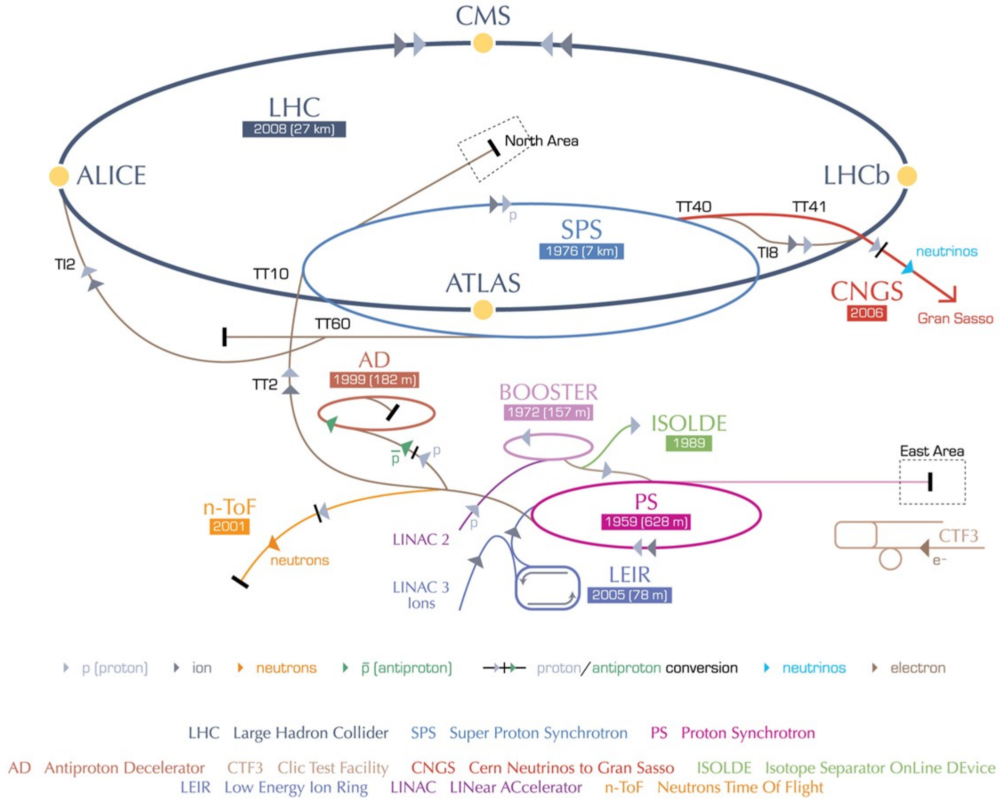

Figure 2.1: The schema of CERN accelerator complex. The image from [22].

2.1 ATLAS Detector

The ATLAS detection system [19] (fig Fig. 2.2) has been designed to be able to detect and measure all stable particles, which could be produced during pp collision (except neutrino). The detector has cylindrical shape with the beam-line as centerline. The detector volume covers almost whole 4π of spatial angle around the interaction point (IP).

The right-handed cartesian coordination system is defined by the z-axis identical with beam-line, and x-axis pointing into middle of LHC ring. The origin of coordination system is in the middle of detector, where the collisions should take place and also there should be collision center of mass.

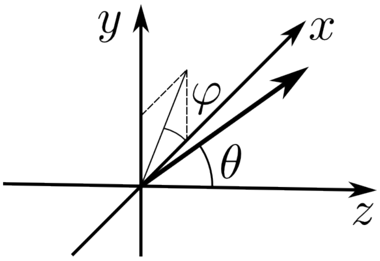

Figure 2.3: Schema of coordination system of ATLAS detector.

The xy-plane is called transversal and z-axis is called longitudinal. Also there is possible and often practical to use spherical or cylindrical coordination system. The cylindrical system is defined by transversal angle φ and distance $R = \sqrt{x^2 + y^2}$ in transversal plane plus z-axis. The spherical coordination system is defined by transversal angle φ, longitudinal angle θ and spatial distance $\rho = \sqrt{x^2 + y^2 + z^2}$ from detector center.

Several of kinematic quantities will be defined now based on cylindrical coordination system. Following notation will be assumed: energy E, invariant mass m, momentum four-vector p and

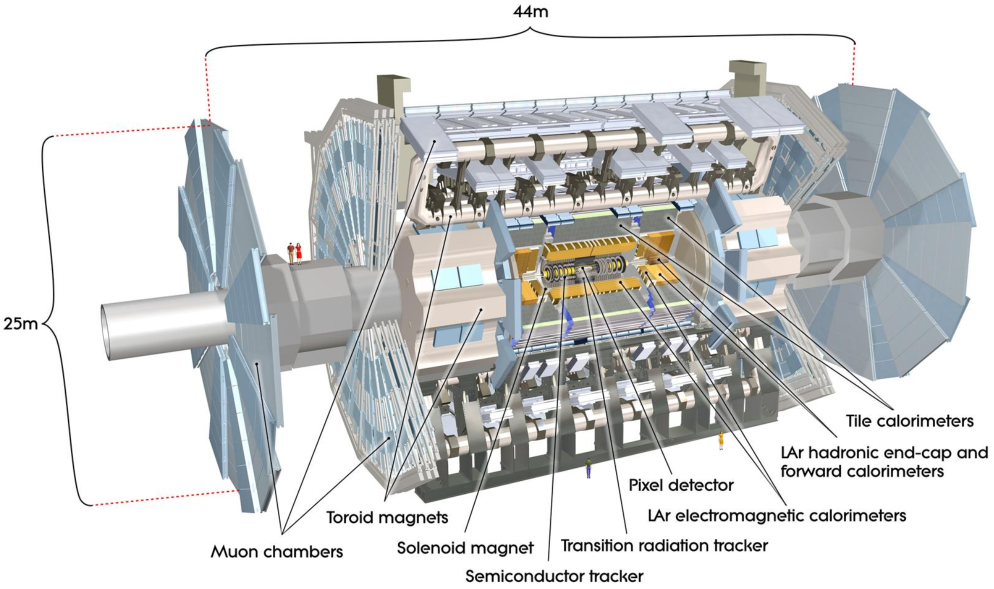

Figure 2.2: The schematic view of ATLAS detector, image from [24].

momentum three-vector $\vec{p}$.

The three-vector of momentum could be described by $\vec{p} = (\vec{p}_T, p_z)$, where two-component vector $\vec{p}_T$ is called transversal momentum and represents the momentum projected in transversal plane, i.e. $\vec{p}_T = (p_x, p_y)$. Since transversal momentum is conserved in collisions and it is equal to zero before collision, the final transversal momentum of the system after collision should zero as well.

As has been mentioned before, the neutrinos can not be detected directly by ATLAS. But they are measured as imbalance of transversal momentum. The useful variable quantizing this imbalance is called missing transversal energy and it is defined as

$$E_{\mathrm{T}}^{\mathrm{miss}} = -\sum_i \vec{p}_T^{(i)} \tag{2.1}$$

where i goes over all detected particles in event. Another detector-related variable H_T is defined as sum of all jets and leptons transversal energy $E_T = \sqrt{|p_T|^2 + m^2}$.

Among frequently used kinematic variables it could be found the rapidity, which is defined as

$$y = \frac{1}{2} \ln \left(\frac{E + p_z}{E - p_z} \right) \tag{2.2}$$

In case of high-momentum (or low-mass) particles the rapidity is asymptotically the same as pseudorapidity, which is defined by

$$\eta = -\ln \tan(\frac{\theta}{2}) \tag{2.3}$$

Often used description of spatial angle is expressed by metric in η–φ space. The standard space separation is

$$\Delta R = \sqrt{\Delta\eta^2 + \Delta\varphi^2} \ , \tag{2.4}$$

where $\Delta\eta$ and $\Delta\varphi$ are separation in transversal angle and pseudorapidity, respectively.

The ATLAS detector consists of four detection parts: inner detector, electromagnetic and hadronic calorimeters and muon chambers. Each detector is most efficient when it is hit by a particle perpendicularly. Therefore each detection part is divided into the barrel region, where the sensitive volume is parallel to beam-line, and the end-cap region, where the sensitive volume is radially oriented.

The particles produced in collision pass through the volume of detector and they leave specific response in active medium of sub-detectors. By the overall signal it is possible to identify the particle (see Fig. 2.4).

Light charged particle like an electron is detected while they pass through inner detector and they are stopped in electromagnetic calorimeter, where the consigned energy is measured.

The heavier charged particle like a proton is also detected by the inner detector and electromagnetic calorimeter, but they are stopped as far as in hadronic calorimeter.

The muons are charged, consequently they are detected in inner detector and then they pass trough all the detector volume. They are only particles, which could reach the volume of muon chambers.

The neutral heavy and strong interacting particles like neutron are not detected by inner detector nor the electromagnetic calorimeter, but they are measured and stopped in hadronic calorimeter.

The massless photon as neutral particle has no hit in the inner detector and it is detected as electromagnetic shower in electromagnetic calorimeter, where all its energy is absorbed.

The last but not least is neutrino – neutral, massless and weak-only-interacting particle. The neutrinos are not detected directly, but only as imbalance in overall transversal momentum.

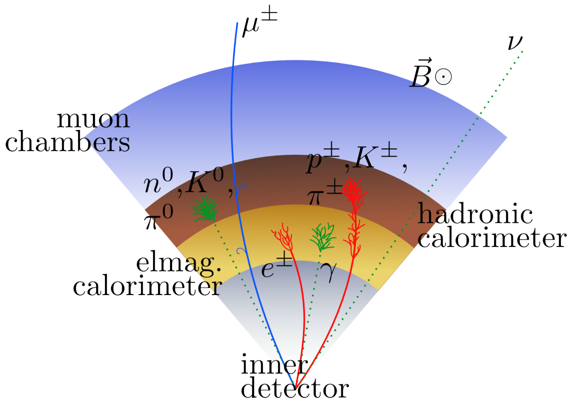

Figure 2.4: Particle identification schema of ATLAS detector. The different particle leaves different signal while passes through the detector volume. See text for description.

If the charged particle moves perpendicularly to magnetic field, the particle trajectory is bended. The bending direction depends on direction of magnetic field and on sign of particle's electric charge. Consequently this is method how to distinguish between charged particles and their anti-particles (they differs only by their sign of electric charge). On Fig. 2.4 the field points towards the reader and therefore the blue lines represents positive particles and red lines negative particles.

Moreover, the bending radius is related to the momentum of particle and the field strength. If the we can provide time-constant magnetic field we are able to measure the particle momentum.

This is the spectroscopic method used by the ATLAS detector. The magnetic field is provided by solenoid and toroid magnets.

The solenoid magnet is situated between inner detector and electromagnetic calorimeter and it provides the longitudinal magnetic field of 2 T for particles inside inner detector. To be able to produce field strong like this the coil of electromagnet is made from NbTi superconducting cables conducting electric current 7.7 kA. Operating temperature of ATLAS solenoid is 2.7 K and the cooling medium is liquid helium with flow 7 g/s.

The toroidal magnet provide radial magnetic field and therefore charged particles are bended towards or away from the beam-line. This is useful in forward region, where solenoidal field has not enough strength. Especially the high-η muons are sufficiently bended in order to measure their momentum.

There are three toroidal magnets on ATLAS, one barrel toroid and one end-cap toroid on each side. The barrel toroid with outer diameter 20.1 m and length 25.3 m is a part of muon chamber system. The electric current of 20.5 kA provides peak field of 3.9 T. Also inside toroidal magnets has been used the NbTi superconducting wires. Because of higher electric current than in solenoid, the operating temperature is 1.9 K with liquid He coolant flowing 410 g/s.

The end-cap toroids are smaller and situated on outer-sides of electromagnetic calorimeter. The parameters of superconductors are the same as in case of barrel toroid but due to smaller dimensions the magnetic field peaks at 4.1 T.

The description of each sub-detector basic properties will be provided starting with the nearest to interaction point – the inner detector, and ending with the outermost muon chambers. If no other specification will be presented, the detector properties has been found in [19] will be followed if not mentioned otherwise.

2.1.1 Inner detector

The inner detector is three-type detection assembly, where each type has barrel (co-centric cylinders) and two end-cap (beam-perpendicular disks) units. It is a tracking and vertex-finder system capable of detection of all charged particle with $p_{\mathrm{T}} > 1\,\mathrm{GeV}$ in region of $|\eta| < 2.5$.

Pixel detector Only 50.5 mm from beam-line center is situated the first of three layers of the pixel detector (Pixel). The Pixel is precious tracking semiconductor detector consisting of 1744 modules. Each module contains active area of $6.04 \times 1.64\,\mathrm{cm}^2$ with pixel size $50 \times 400\,\mu\mathrm{m}^2$, where the better spatial resolution in transversal plane. As a result the resolutions are $\sigma_\varphi = 10\,\mu\mathrm{m}$ and $\sigma_z = 115\,\mu\mathrm{m}$.

Basically, the pixel is P-N junction connected to 600 V reverse voltage. When particle passes through the pixel, it ionizes the semiconductor volume. This produces electron–hole pairs and the charge is collected by electrodes. Each pixel is connected to the amplifier followed by discriminator with adjustable threshold.

As innermost device, the Pixel has the most irradiated electronics among all detectors. The approximate operating temperature of Pixel modules is $-10\,^{\circ}\mathrm{C}$.

Semiconductor tracker The SCT consists of four barrel layers with 2112 modules and 18 end-cap disks with 1976 modules covering $|\eta| < 2.5$ situated outside the Pixel.

Each SCT module has back-to-back strip sensors mounted on read-out electronics. The detection principle is the same as in case of Pixel detector, but the spatial arrangement is different. The SCT sensor is formed by p-in-n microstrips with pitch $80\,\mu\mathrm{m}$ and the strips on doublet of module sensors are rotated to each other to provide position measurement.

The sensor resolution is $17\,\mu\mathrm{m}$ in lateral $(R - \varphi)$ plane and $580\,\mu\mathrm{m}$ in longitudinal (z or R) coordinate. Operating temperature is $-7\,^{\circ}\mathrm{C}$ and collecting voltage is $350\,\mathrm{V}$.

Transition radiation tracker The last and outermost part of inner detector Transition Radiation Tracker (TRT) is basically purposed for electron identification. The TRT consists of 73 fiber–straw layers in barrel region and 160 foil–straw planes in end-cap region. It is able to detect charged particles with $p_T > 0.5\,\mathrm{GeV}$ and $|\eta| < 2.0$ except barrel–end-cap transition region $0.8 < |\eta| < 1.0$.

The transition photon is created when charged particle crosses the boundary of two materials with different electron densities[1]. The photon emissivity depends on Lorentz γ-factor of incident particle. The photon is in TRT measured by proportional drift tubes filled with Xe-rich gas mixture to provide good detection efficiency.

The tubes are operating at voltage $-1530\,\mathrm{V}$ with tungsten anode wire coated with gold. The drift time and wire position provide $\sim 130\,\mu\mathrm{m}$ resolution in $R - \varphi$ plane.

The bending of particles trajectories in inner detector is provided by solenoid magnet. The momentum resolution depends on spatial resolution of detectors and stability of magnetic field. The required momentum resolution (momentum in GeV) of tracking system alone was designed to be

$$\frac{\delta p_{\mathrm{T}}}{p_{\mathrm{T}}} = 0.05\% p_{\mathrm{T}} \oplus 1\% \tag{2.5}$$

2.1.2 Calorimeters

The most important property of calorimeter is hermeticity, which means it provides full acceptance and enough depth to stop all particles in calorimeter volume. The ATLAS calorimetric system is divided into hadronic and electromagnetic part, where both have full φ coverage.

The electromagnetic calorimeters absorb γ mainly by pair-creation, Compton scattering, photoelectric effect, and $e^{\pm}$ mainly by bremsstrahlung and ionization. The incident high-energetic

---

[1] More detailed explanation of transition radiation could be found in PDG.

particle creates electromagnetic shower, which is combination of several following pair-creation–bremsstrahlung processes. The length of this shower depends on energy of the incident particle and the absorber material of the calorimeter.

The hadronic calorimeters profits from the electromagnetic processes, and also from so called hard-nuclear processes invoked by strong interaction. As was written in Sec. 1.1.1, if one tries to pull the quark out of a hadron, the energy, needed to done this, is transformed into creation of new quark pair from vacuum and new hadron on both side of gluon string is formed. This is usually repeated until the energy of incident particle is bellow the quark-production level. As the result of this phenomena is spatially-correlated shower of hadrons called jet. The primary purpose of hadronic detector is to absorb and measure all jets from collision.

Electromagnetic calorimeters The ATLAS electromagnetic calorimeter is divided into cylindrical-shaped barrel and disk-shaped end-cap with acceptance $|\eta| \leq 1.475$ and $1.375 \leq |\eta| \leq 3.2$ respectively. Both parts consists of units (towers) operating at low temperature ($\sim 85\,\mathrm{K}$) due to liquid argon (LAr) presence. The tower is designed as sampling calorimeter with accordion geometry. The active medium is liquid argon (4 mm) zig-zag-interlaced with lead plates (2 mm) giving the $25\,\mathrm{X}_0$ radiation lengths for 38.9 cm thick calorimeter.

The energy resolution (in GeV) could be described as square root of quadratic sum of several terms

$$\frac{\sigma}{E} = \frac{a}{\sqrt{E}} \oplus \frac{b}{E} \oplus c \tag{2.6}$$

where each parameter need to be estimated experimentally during test-beam and also during every-run calibration process. Stochastic term has been estimated to $a = 11\%$, sampling term is η-depended and the value is in range $9\% < b < 22\%$. The local constant term is $c = 0.5\%$ for barrel and $c = 0.7\%$ for end-caps. The spatial resolution is $\Delta R = 0.025 \times 0.1$ for barrel and $\Delta R = 0.025 \times 0.025$ in end-cap region, where ΔR is defined in Eq. 2.4.

Hadronic calorimeters Outside the electromagnetic calorimeter it is assembled hadronic calorimeter. The acceptance is $|\eta| < 1.7$ for barrel, $1.5 < |\eta| < 3.2$ for end-cap regions. The additional forward hadronic calorimeter for high-pseudorapidity range $3.1 < |\eta| < 4.9$ is also present.

The barrel hadronic calorimeter (TileCal) is built from tiles containing steal absorber and plastic scintillator pads connected by wave-length-shifting optic fibers to photomultiplier tubes. The narrowing-to-center tiles are mounted side-by-side to form cylindrical structure around electromagnetic calorimeter.

The energy resolution (in GeV) of Tile calorimeter is described by

$$\frac{\sigma(E)}{E} = \frac{a}{\sqrt{E}} \oplus b \tag{2.7}$$

where the $a \sim 10\%$ and $b \sim 0.17\%$ has been fitted from test-beam measurements and the symbol "$\oplus$" symbolize square root of quadratic sum.

Hadronic end-cap calorimeter (HEC) is copper–liquid-argon plate-sampling calorimeter. The plates are perpendicular to beam-line and grouped to two disks, which are radially divided into 32 wedge-shaped modules.

The energetic resolution has the same dependence as for TileCal Eq. 2.7, where stochastic term a has been determined to be 71% and constant term $b = 5.8\%$. The spatial resolution is given by granularity of calorimeter pads and it is $\Delta R = 0.1 \times 0.1$ in region $|\eta| < 2.5$ and $\Delta R = 0.2 \times 0.2$ for larger η.

The end-cap Forward Hadronic calorimeter (FCal) provides additional energy measurement for high η region. The FCal is situated within HEC and consist of three layers: FCal1 – basically electromagnetic copper-LAr, FCal2 and FCal3 - tungsten-LAr sampling calorimeters.

There are three disks with generally the same multi-rod electrode geometry. The electrodes are parallel to beam-line and they are made from copper in FCal1 and from tungsten in FCal2&3. The absorber medium is copper (tungsten) for FCal1 (FCal2&3) and the depth of whole FCal is $\sim 10\,\mathrm{X}_0$. The energy resolution has the same relation as for TileCal Eq. 2.7, where stochastic term a has been determined to be 28.5% (94%), constant term b is 3.5% (7.5%) for FCal1 (FCal2&3) and energy is in GeV. The FCal designed spatial resolution is $\Delta R = 0.1 \times 0.1$ in front and $\Delta R = 0.2 \times 0.2$ in back disks [25].

2.1.3 Muon Chambers

The muons, as heavy leptons, much less ionizes the volume of whole detector than electrons and do not interact strongly. This properties distinguish them from the other particles and they can be detected as the only particles which escapes from calorimeter. On ATLAS there are several muon detectors.

In barrel region Monitored Drift Tubes (MDT) provide tracking system in $|\eta| < 2.7$ triggered by Resistive Plate Chambers (RPC). The end-cap region $2 < |\eta| < 2.7$ is formed by triggering Thin Gap Chambers (TGC) and additional tracking detector the Cathode Strip Chambers.

Monitored Drift Tubes The MDT are muon precision-tracking chambers with acceptance $|\eta| < 2.7$ and full φ angle. There are three layers in barrel region, where tubes share the volume with toroidal barrel magnet. In end-cap region the MDT consists of one disk before, one above and one right behind the end-cap toroidal magnet. The fourth, outermost disk of MDT in distance 21.84 m from detector center is the outermost part of whole detector.

The tubes are filled with pressurised noble gas mixture. Gold-plated tungsten-rhenium wire in the center is working as collecting anode. While the muon moves inside the tube the gas is ionized and free charge is collected to the anode. The death-time 700 ns is derived from maximal charge-drifting time and due to radial electric field is almost independent on angle of incident particle or position in tube.

The distance wire–track in tube is calculated from time shape of the measured signal. The toroidal field bends the track of muons in R–z plane, where the MDT has spatial resolution $\sigma_z = 35\,\mu\mathrm{m}$ and consequently it is able to measure the momentum with resolution $\frac{\delta p}{p} = 0.09p$, where p is in TeV.

Resistive Plate Chambers The triggering system for MDT in barrel region $|\eta| < 1.05$ is provided by Resistive Plate Chambers (RPC). There are three layers RPC modules appended to MDT module and as the name says there is no wires in RPC, but resistive plates in hydrocarbon-derivatives-gas mixture. The parallel arrangement provides the spatial resolution $\sigma_z = 10\,\mathrm{mm}$ and $\sigma_\varphi = 10\,\mathrm{mm}$. As the triggering detector the time resolution $\sigma_t = 1.5\,\mathrm{ns}$ is also important and it is influenced mainly by drift of charge. The RPC are able to trigger muons with momentum down to 5 GeV.

Cathode Strip Chambers The addition innermost muon tracking in end-cap region $2 < |\eta| < 2.7$ is provided by one disk of Cathode Strip Chambers. The CSC is multi-wire noble-gas proportional chamber with radially oriented wires and two cathode strip layers perpendicular to each other.

As the muon passes trough the volume it ionizes the gas and creates the free charge which is attracted to the strip cathodes. The transversal position is interpolated from charges induced on neighbouring strips. The transversal resolution is $\sigma_R = 40\,\mu\mathrm{m}$ and $\sigma_\varphi = 5\,\mathrm{mm}$.

The maximum drift time due to vanishing drift field near two cells has an effect of the long tale in distribution of the arrival time. By the electronic logic only leading electron signal is taken into account and the resulting time resolution of CSC is $\sigma_t = 7\,\mathrm{ns}$.

Thin Gap Chambers The end-cap muon triggering is provided by Thin Gap Chambers (TGC) with acceptance $1.05 < |\eta| < 2.4$. Except the triggering the azimuthal coordinate is measured as additional information for MDT end-caps. The TGC is multi-wire proportional chamber filled with hydrocarbon gas mixture.

The unit of TGC has tree or two chambers separated by insulating honeycomb-layer. In gas volume are anode wires surrounded by graphite layer, while there are the cathode strips from outer side. This provides resolution $\sigma_R = 2 - 6\,\mathrm{mm}$ $\sigma_\varphi = 3 - 7\,\mathrm{mm}$. The death-time of detector and electronics give the time resolution $\sigma_t = 4\,\mathrm{ns}$.

2.2 ATLAS trigger system and data acquisition

Physically interesting events are not produced in every collision and not every collision could be stored. Therefore it has been needed to design the system, which selects as much and as interesting events as possible. The ATLAS trigger and data acquisition (TDAQ) is structural filter system for choosing interesting events and storing the measured data. The trigger system has three selection levels: Level-1 (L1), Level-2 (L2) and Event Filter (EF). The L2 and EF together form the High-Level Trigger (HLT). The schematic view of TDAQ system is on Fig. 2.5 with designed trigger rates followed by rates for year 2010 and 2011.

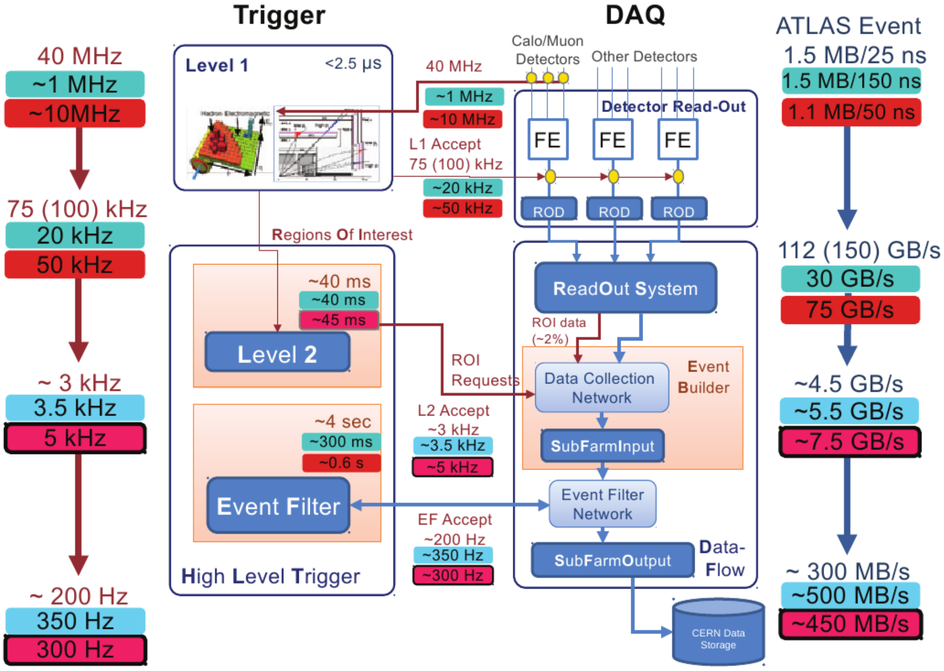

Figure 2.5: Schematic view of TDAQ system with rates from [26]. The labels without background, with blue and red background are designed, year 2010 and year 2011 trigger rates, respectively.

2.2.1 Level-1

The ATLAS bunch-crossing rates has been $\sim 10\,\text{MHz}$ in year 2011. The first decision is provided by custom built electronics, where the algorithms of L1 trigger has been implemented. The output trigger rates $\sim 50\,\text{kHz}$ was changing during the year. The all L1 electronic is mounted as near as possible to read-out devices of sub-detectors considering radiation protection of trigger electronics.

The L1 is selecting events and is searching for region of interest (RoI) in measured data from muon trigger chambers and all calorimetric systems. The searched objects of interest are high-p_T muons, electrons/photons, jets, τ-jets and large $E_{\mathrm{T}}^{\mathrm{miss}}$. The Central Trigger Processor (CTP) is decision and control unit of L1 system. Besides event filtering the CTP controls timing of triggers, detector read-out and distribution of data to next levels of TDAQ.

The L1 muon processing unit searches for muon candidates using information from RPC in barrel and TGC in end-cap regions. After coincidence on several levels of triggering chambers the p_T thresholds are applied. If the muon candidate fulfil the p_T cut the information of position in terms of η and φ is send to Central Trigger Processing unit. Up to seven muon multiplicities are manageable by L1 and the higher numbers are described by maximal values.

The other L1 objects of interest are calorimeter-related. After analogous processing of signal from calorimeter sub-parts the digitalization and correction to bunch-crossing is provided by pre-processors. The digitized data are sent to two algorithmic processors: jet/energy processor and cluster processor. The jet/energy processor (JEP) looks for missing transversal energy and jets by fast sliding window technique. The output from JEP to CTP is the sum of transversal energy, missing transversal energy and jet-multiplicities. The clustering processor (CP) is finding clusters, which could be created by electron/photon and τ jets and then it sends their multiplicities to CTP. Both muon and calorimeter processing units provide RoI directly to L2.

The Central Trigger Processor collects overall information about the event and made final decision of L1 system. Except mentioned muon and jet L1 units there is information from bunch-crossing triggers, beam-pickup monitors and minimum-bias scintillation counters. Several triggering thresholds are remotely modifiable and the CTP makes final decision as logical OR of 256 trigger items.

2.2.2 High level trigger

The next filtering procedure is done by Level-2, which decides whether it is needed to transfer data-stream from Read-Out Drivers (ROD) to surface computing farm by gigabit ethernet network. The L2 is software based trigger system which reduces rates from 50 kHz to 5 kHz. The computations are provided on L2 processing farm, which performance is highly configurable.

The L2 starts with RoI from L1 and it combines RoI with the information from other detectors. There are physically-related sequences of criteria called trigger chains. The event is reconstructed to obtain the basic physical objects (feature extraction) and decision is made at each step to improve processing time.

The data are sent to CERN central data-recording facility by EF output modules (SFO) after application of the selection criteria. The events are incoming unsorted and each SFO works independently. All fragments are merged into a complete event during process of event building. The SFO output is controlled by supervisor unit and then the final data-stream is produced.

As a result there are several physical data streams for electrons, muons, jets, photons, $E_{\mathrm{T}}^{\mathrm{miss}} + \tau$ and B-physics. These streams contain full event information in contrary to calibration and express stream, where only necessary information for the calibration and data-quality is stored.

Data acquisition system "waits" until the trigger decide if the event is suitable for storage. During that time the data from detector are stored in buffers. When the L2 and EF decide to store, the data are transfered and stored as RAW files on magnetic tapes accessible from Tier-0 site. The later procedures with data are described in next chapter.

The set of trigger settings forms trigger chain. When the rates for some trigger settings are too high, the triggers are pre-scaled. Pre-scaled factor is a number of events which will be automatically skipped in chain without processing. In addition the trigger chains and pre-scale factors form trigger menu. Since the detector is not always 100% functional the monitoring system of detector conditions and performance is provided. The database of runs and lumiblocks[2] suitable for physical analysis – Good Runs List (GRL) – is created and together with trigger menu and pre-scale factors has been used for luminosity calculation.

---

[2] The lumiblock is period of approximately three minutes of data taking. The instantaneous luminosity is expected to be constant during the lumiblock.

Chapter 3

Computing software

A huge amount of high-precision measurements are recorded by the high energy physics experiments. Moreover, numerous simulations of physical phenomena are needed. As a result, there is strong demand to store huge amount of data and analyse them as quickly as possible.

Recording, storing and processing of the data is split into several stages and each stage is provided by different software framework. The computing software and processing of data used in our analysis is described in this chapter.

The official tools (data, simulations or selection criteria) in this work will be understood as tools, which has been adopted from top physics group of ATLAS experiment. Consequently it is possible to compare the results between subgroups and eventually point out the insufficiencies or mistakes.

3.1 Official ATLAS software framework

Since each physical analysis is different, the different computation tools are needed. However, many tools are mutual for many physical groups or analysis. The consistency of data, computations and results is guaranteed by code centralization.

3.1.1 Athena framework

The Athena framework is official wide-range software framework, which has been developed by and for ATLAS collaboration [27]. All computations, from high level trigger to final analysis histograms, has been implemented into Athena. Therefore it is complicated and highly sophisticated juggernaut, which consists of ~ 5 millions lines of source code [28].

The kernel of Athena is based on Gaudi [29], which is framework originally developed for LHCb experiment. Major structure of Gaudi was kept by ATLAS developers and adapted for requirements of the ATLAS experiment. The Athena is basically written in C++ with some parts of FORTRAN code (wrapped by C++) and visualization applet written in Java. For custom parameters, settings and controls there are JobOption files written in Python, which forms flexible Athena front-end.

Structure of Athena has been designed to be able to implement all necessary algorithms by object-oriented abstract model (Fig. 3.1). The Application manager takes care of program running, driving and terminating. There is only one instance of Application Manager per application and it is common for all components.

The basic widely-used structure of high-energy-physics application is formed by Initialization, Loop and Finalization. The Initialization stage is used for declaration of the objects and initializa-

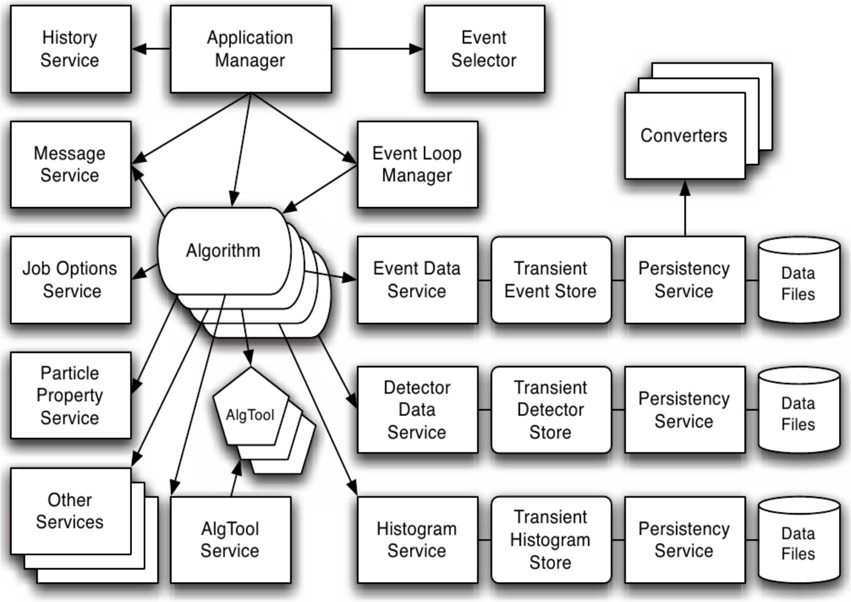

Figure 3.1: Athena internal structure

tion of their values, but also calculation are sometimes needed in this stage. The Loop stage is the main stage of program and usually contains procedures which are repeated many times (usually per event). Finalization is stage suitable for the results saving and after-processing calculations. This application structure is also used in the Athena framework.

The Algorithms are the basic components for per-event computations. For easier manipulation with Algorithms there is Sequencer, which contains several Algorithms or another Sequencers. The Tools are similar to Algorithms, but they can be executed more than once per event, and usually they are part of Algorithms or Services.

The Services provide supporting code for physical analysis like messaging system, graphical output, random numbers generators etc. The Transient and Permanent Data Storage systems are major components and all necessary operations with data are implemented in these components. The conversion of the data from one type to another is provided by the Converters. Since the selection of events or data information is needed, the Selectors are implemented for these purposes in the Athena.

The set of source code, which forms logical unit is encapsulated into the package. The Packages are grouped by topics and stored in folder structure. Software versioning is provided by revision control system SVN [30]. Building of source code, version dependency and testing of new developing code are provided by Code Management Tool (CMT) [31].

As will be explained later (Sec. 3.1.2), for physical analysis of collisions it is need to have generators – computational tools, which predicts the result of collision based on physical theory.

Generators needs input parameters and distribution functions to provide as right predictions as possible. Each Monte Carlo generator is suitable only to specific process. Therefore, all officially used generators and their parameters are embedded in the Athena. Moreover, it is sufficient for users to work only with JobOption files, where all necessary options for event generation could be set. Official generators and settings used in our analysis are described in Sec. 4.2.

Generation is followed by simulation of particle pass through volume of detector and signal modeling. For basic interaction of particles with matter there is standard program GEANT4, which is incorporated into Athena. Because the precision is question of alignment of detector as well, there is computational model of ATLAS detector describing the same state as could be found the real detector in cavern. The GeoModel [32] is format used for description of all detector parts (including construction and shielding) by geometrical primitives ($\sim$ 30 millions parts [28]) and material properties.

Since the computation of detector response is time-consuming process, there is faster algorithm called AtlFast-II [33]. The most elaborated is simulation of calorimeter response, therefore parametrised particle showers (FasCaloSim) and simplified detector description for tracking system (FATRAS) are used in AtlFast-II algorithms. As a result the algorithm is almost 10 times faster than the full GEANT4 simulation, but different correction factors are need to be applied, which has been naturally done in our analysis.

We have used Athena framework only indirectly (the Data and Monte Carlo files) and directly only few packages, which could be used outside the Athena e.g. GoodRunLists, D3PDReader, etc.

3.1.2 Event Data Model

To satisfy all needs around data processing the Event Data Model (EDM) has been developed for ATLAS data files. The EDM not only contains the description of file types but also the procedures of their creation. This model, defined in Athena packages, will be introduced on next lines. The full description could be found in [27].

If the analysis is provided on raw data from detector electronics (RAW), the time necessary for loading and processing will be inadmissible. There are information which are needed for all groups and there are as well highly specific information, which are necessary only for few analysis.

As a result there are several stages of data types, which size is reduced until the files contain only needed information. Not only physical analyses are provided on measured data. Also calibration, performance and data quality studies are accomplished. In summary different file types are used for different kind of analysis. Three basic concepts of reducing the data size are:

Skimming removes the events which not passed our selection criteria.

Thinning removes whole objects (e.g. TTree) which not contains wanted information.

Slimming removes properties which are not more needed inside objects.

Before data file type description is reasonable to mention Monte Carlo simulation procedure.

SIM The prediction of the results of experiment is challenging. Commonly used method is based on Monte Carlo (MC) method [34]. The Monte Carlo method is frequently used in experimental physics. One can model the whole experiment by knowledge of probabilities partial effects (spatial distribution of outgoing particle, probability of creating signal in detector etc.). Starting point of modeling is random number generator with known or expected distribution. Each one random number represents possible result. Consequently the expecting measurement results could be obtained by adequate repeats of random number generation.

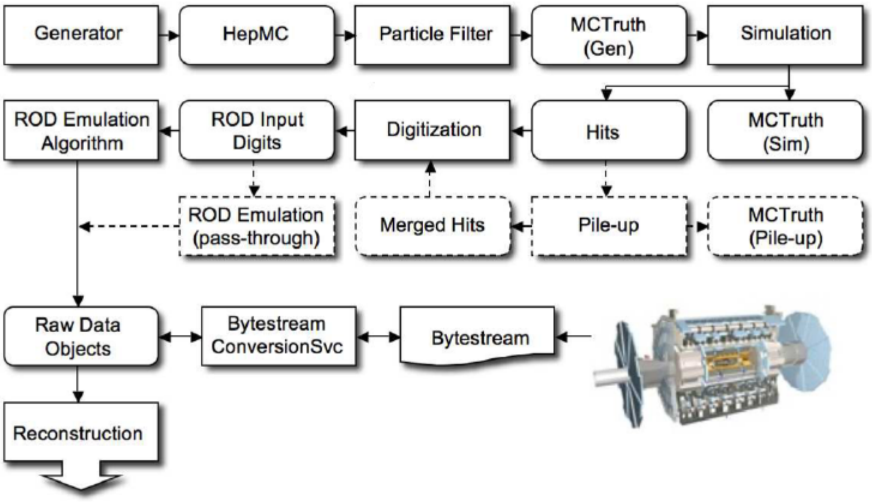

Figure 3.2: Stages of Monte Carlo modeling of event in Athena framework, with depicted the real input from detector. Figure from [35].

Modeling of the experimental results typically has two stages. In first stage – event generator – the result of physical process (like products of collision) is simulated by theoretical predictions. Usual output of event generator are four-momenta of particles, their vertex of origin and other relevant physical properties like type[1], mass, charge, spin etc. The second stage – detector simulation – starts from generated particles from first stage. The flight of the particles through detector is simulated. The complete geometry and material properties of detector are need. Moreover for higher precision the effects in detection electronics could be simulated also. As the result of detector simulation is the expected signal in same format as in real measurement. In Athena this two-stage process of modeling is much more sophisticated (see Fig. 3.2).

---

[1] Type (or kind) of particle is in generator level symbolized by integral number. The list of particles and their identification numbers could be found in PDG.

The whole process of generation simulation and digitization is now automated and simply accessible from Athena by so callled full-chain analysis. Usually it is one of the first exercises, which are introduced to newcomers due to its automation and user-friendliness.

The event generators are based on physical theories. As same as theoretical models have limits, also generators, built-up from these models, are more or less suitable for specific physical process. In Athena could be found remarkably large numbers of event generators, which parameters could be tunned. The generators used in our analysis are described in Sec. 4.2.

The crucial factor of detector modeling is knowledge of detector status and alignment. Full description of detector is stored by GeoModel and the passing through detector is simulated by GEANT4 using the information from GeoModel. Owing to this procedure is time-consuming, especially for calorimetric parts, there are faster algorithms performing simulations, when the high precision is not needed, e.g. AtlfastII.

Output of simulation is the same filetype as output of real experiment electronics (RAW), but with additional “truth” values. From this stage the analysis for data and Monte Carlo are almost identical. The change from truth values to results is used for corrections, unfolding and performance studies.

RAW As was mentioned on very beginning of this chapter, there is huge amount of data, which needs to be processed. Not every event can be stored and different groups needs different events and information for their analysis. First “filter” of data is trigger (described in Sec. 2.2). The trigger decide which events are interesting and send command to save all output from all detectors.

When the event filter decide to save the event, the byte-stream output of detector is transferred to Tier-0 tapes where the events are stored in $\sim 2\,\mathrm{GB}$ files. One event had 1.1 MB in year 2011 and trigger rate has been increased during the year from 200 Hz to 400 Hz. The long term storage replicas of RAW data are created and stored on Tier-1 sites. To be able to store more data the RAW files has been compressed to size 0.66 MB/event [36]. Due to no physical analysis can be provided with the RAW data, the files needs to be transform into Event Summary Data files (ESD).

Event summary data The output of event reconstruction is stored in Event Summary Data files. The idea is to use RAW data again just for re-reconstruction or calibration and for all other analysis the ESD files have to be sufficient. Because of that, ESD contains all information about the event stored in POOL ROOT format with size 1.21 MB/event.

The first production of ESD files takes place at Tier-0. Additional procedures are provided on Tier-1 sites and files are then distributed on GRID. The creating of ESD replicas depends on needs and potential of each GRID site. Besides special case (events with Higgs candidates), all ESD are short-term files stored only during AOD production or first reprocessing.

Analysis Object data The first suitable level of file size and structure for physical analysis is provided by Analysis Object data files (AOD). The production of AOD files does not need much processor resources, and it takes place on Tier-0 for first-pass reconstruction with additional operations on Tier-1 sites. The size of one event in AOD file is $\sim 0.16\,\mathrm{MB}$ for year 2011 and it differs according to streams. The stream is set of events related to physical or performance group.

The different AOD file is created for different streams and it can happens that one event is stored in several streams. Therefore each event has unique identifiers: run number and event number. This identification makes possible to find event multiplicities or helps with comparing two reprocessed files.

Other output beside AOD production are TAG files, containing event level metadata stored as relation databases. This collection of TAG files provide quick finding of interesting samples in low-sized files and together with GoodRunsLists also luminosity could be calculated.

Derived Physics Data The outcome of AOD file derivation process are Derived Physics Data (DPD). There are several levels of derived data and the highest (most compact) D3PD has format of standard ROOT TFile with TTree. An advantage of D3PD files is that the TTree are saved with relation tables. Consequently it provides faster browsing and matching the items inside the branches.

The D3PDs could be found on GRID and also could be created by D3PDMaker package from RootCore or Athena. The top D3PD contains braches with trigger information, physical analysis objects, the primary vertex and tracks information. In case of Monte-Carlo D3PD there is additional information about generated particles.

3.2 Distributive computing on GRID

Because most of physical calculations claim a lot of mathematical operations, it is more favourable to provide distributive computing (multi-tread processing). Basically it means that the analysis is divide into independent procedures, which are run on several computation nodes simultaneously (usually the looping through events). Then the outputs from all nodes are merged together. As a result computational time is much lesser than in case of one-thread processing.

Due to reasons mentioned above, it has been created world-wide distributed computing system GRID, which provides access to enormous size of storage area ($\sim$50 PB [36]) and numerous computation cores ($\sim 10^5$ [36]). The grid joins the largest computer farms all over the world (about 130 sites [36]), consequently users can access them independently of their geographical position.

Event storage process of the ATLAS detector is divided into tree hardware levels (Tiers). The Tier-0 is located in CERN and stores events which were selected by trigger system onto magnetic tape, also first reconstructions of events and calibrations are provided by Tier-0. Moreover the replicas for reconstruction reprocessing are copied from tape to 10 regional Tier-1 centres, which also provide the long-term protection against possible data loss.

The Tier-2 is divided into clouds including about 80 computational sites. The data are encapsulated on sites in datasets and database with information about all datasets from all sites and their content is available for end-users. The sites are divided into computational nodes, which are usually virtual operating system with same environments as were used for developing the code.

The Tier3 is a new concept of off-Grid distributive computing provided on institutional or university farms. The same middleware as on GRID is used on these farms. The most prospective services on Tier-3 farm is PROOF (Parallel ROOT Facility). It is system of working nodes which are control by master node and number of cores is controlled by user. We have access to PROOF farm in Kosice and there is plan to use it in future analysis.

The grid is not only used by high energy physics. Also other scientific disciplines has requirements for computational and storage capacities, e.g. biological simulation of organisms, the prediction of tectonic movements in geography, various mathematical simulation and numerical computation etc. That means lot of people with not equal data permissions and computational time.

Moreover, there are three GRID networks using different middleware and user-access databases: American VDT, Scandinavian NorduGRID, Europian and others DataGrid.

To be able to use full-capacity of these three networks for every user there has been designed Virtual Organization Management System (VOMS). It is database of user certificates, which provides information of data and computing permissions per each user. Furthermore there is also priority index for every users, which support effective distributive computing and fair user policy.

Generally processing of the data has higher priority and Monte Carlo simulations are run whenever is possible.

The main idea is to be as effective as possible. Therefore motto of GRID is “Send kilobytes to petabytes, not petabytes to kilobytes”, which means that the source code is sent to site where are the data and not vice versa. Some of the data are stored on several places simultaneously, so called replicas. Then it is up to user to deiced to which site the code will be submitted.

The program itself is run by middleware – dealer software which works on principle of jobs and queues. The middleware provides job control (submitting, deleting, getting a job status), user identification in system (VOMS, certification) and access to information about datasets.

Sending jobs on GRID in our analysis was provided by Production and distributed Analysis (PanDA) system [37]. ATLAS workload management system receives more than 5 millions jobs per week. The Athena framework is installed on working nodes and submitting is provided by command `pathena`. For ROOT jobs (mentioned in Sec. 3.3) submission is used command `prun`.

Our analysis data are stored on GRID and processing has been performed on GRID with official tools (except skimming of `NTUP_TOP` files, which was done by our skimming code discussed later in Sec. 3.4). The main analysis has been provided on Prague farm Golias, which is Tier-3-like farm with own storage element based on GRID storage and resource distribution system TORQUE (Terascale Open-source Resource and QUEue manager).

3.3 ROOT

The object oriented data analysis framework ROOT [38] is widely used tool in high energy physics experiments. It is open-source written in C++ and source code or already compiled packages could be found in [39]. This multi-platform (UNIX/Linux, Windows, Mac) framework contains all what is needed for statistical data analysis.

Internal structure is based on hundreds of classes grouped into 19 modules. The basic element of ROOT is CINT – C interpreter. It is well-known that C++ is non-interpretative programing language, i.e. the compilation of code is need. The CINT is program which works with precompiled ROOT libraries, and it links and loads them while the program is running. The CINT with other ROOT tools make available simple production of graphical outputs from experiment data.

Moreover the CINT allows to users write so called ROOT scripts. This is source code with C++ syntax, which does not contain main function but function of the same name as the file has. When the sequence of commands is written, the user opens the ROOT script file in CINT and the commands are executed by CINT.

General object of ROOT is TObject. The TObject is abstract class from which almost all other classes are derived. Except classes the ROOT contains several variable types and constants. For instance redefinition of real number with double precision Double_t has advantage in multi-platform processing, where ROOT controls the precision of number to be the same on all platforms. Constants like colors and styles are useful for quick changes of output format.

All classes derived from TObject could be saved into TFile. The TFile could be stored on disk usually with .root suffix. Internal structure of TFile is similar to directory system of operation system, but it is readable only by ROOT framework. The TFile class within saving provides updating, deleting, renaming the classes etc. Also user defined objects derived from TObject could be saved. However, before saving/reading own class objects it is needed to load the definition of new class to CINT by ROOT dictionary.

The basic graphical interface of ROOT is the TBrowser. It is user friendly explorer of file system with capability of reading and browsing the ROOT files. The histograms or graphs could be directly draw inside the TBrowser window. Furthermore the TBrowser execution of commands from command line simulator or editing of script files in build-in editor.

Even we use many features of ROOT framework in our analysis it is only small part of full capability of ROOT. Therefore we will describe only few main tools which has been used in our code.

The ROOT TTree is class with tree-like structure for storing set of values (usually measurement results). The TTree has one or more instances of TBranch. The each TBranch represents handler for one variable. The values (entries) in TTree are sorted by index (usually event number) and for each index there is one value per each TBranch. For example one want to store particle kinetic observables p_x, p_y, p_z and identification number id, for each particle there will be one entry in TTree and for each observable one TBranch.

In our analysis has been often needed to pair two trees (e.g. generated and reconstructed). For this purposes is good to use BuildIndex method, where as input there are two branches with unique integral values (e.g. run number and event number). This method creates hash table and therefore it is quicker to find the corresponding index in second TTree.

All graphical output in our analysis has been done by ROOT histograms, function and graphs. The basic graphical output in high energy physics is histogram. Mathematical definition of histogram could be found in Chap. 5. All histogram-like classes in ROOT are derived from abstract class TH1. The histogram could be defined in 1,2 or 3 dimmensions and could be based on several variable types (double, int, char). The name of class is derived right from these two properties: TH – for histogram, number for dimensions and character for type (e.g. S for short, D for double F for float etc.)

Because the histogram is derived from TObject it is possible to save it into TFile. Most frequently used method of histogram is Fill, which increment the value of appropriate bin by one or by weight if is defined. Also comparison algorithms, fitting and basic arithmetic operations are defined for histograms. From numerous tools we mention method GetRandom(), which is used to obtain random number with probability distribution function represented by histogram. This method will be used for creating pseudo-experiment in Sec. 5.3.2.

The work with character strings is not straightforward in C++. In ROOT there is class TString which provides basic operations with text and also TLatex class for implementing the Latex [40] syntax for equations and symbols. Even though it is more comfortable to use interpretive object-oriented language Python. The interface between Root and Python is porvided by TPython class and PyROOT library. This feature gives us ability to call Python objects in C++ code and also vice versa. The PyROOT has been used for histograms finalization and plotting.

Many other experiments on LHC and all over the world are using the ROOT or ROOT-derived frameworks for data processing. The ROOT system of storing the data is so advanced that has been used inside Athena. There is ARA (Athena-Root-Access), which allows to produce the histograms directly from Athena analysis. This is often used Data Quality monitoring and trigger system control.

The ROOT could be used as shared library with user programs. This feature requires to compile user code with additional ROOT flags. Some times this could be little bit tricky, especially in bigger projects. Therefore the ROOT has been implemented into several frameworks like Athena [27], SFrame [41] or RootCore [42]. Also configuration files for CMake [43] compiling system are provided and could be usefull.

3.4 Data preparation

Because we have specific needs for information for our analysis we create our own mini-ntuple ROOT files. The mini-ntuples has been created from official top D3PD files. Due to size of D3PDs $\sim 15\,\mathrm{TB}$ for MC samples and about $30\,\mathrm{TB}$ for data sample, the skimming was needed before downloading the files to the computing servers. It is also possible to run the mini-ntuple production on GRID, but the reprocessing of mini-ntuples has been often needed during the analysis and therefore the skimming was more advantageous.

We create own skimming ROOT script, which is selecting interesting events. Owing not to lose interesting events, looser selection criteria than the official one (see Sec. 4.1) has been chosen for skimming selection.

Firstly, the event must contain at least two "loose[2]" leptons. The electron transversal energy must be higher than $15\,\mathrm{GeV}$ and jet in region $|\eta| < 1.37$ or $1.52 < |\eta| < 2.47$. The muon transversal momentum must be higher than $10\,\mathrm{GeV}$ and muon track in region $|\eta| < 2.5$. Finally the additional cut on missing transversal momentum $E_{\mathrm{T}}^{\mathrm{miss}} > 20\,\mathrm{GeV}$ for Drell-Yan samples are applied.

The skimming procedure reduces D3PD files to about 10% size of original file for signal samples and to even smaller size for background. As a result it was possible to store skimmed files and provide the production of mini-ntuples locally. However, few Athena packages are needed to be able to read and apply corrections on skimmed files. As was mentioned above, there has been the demands to create framework for simpler using of some Athena packages. Moreover, the ROOT is widely used and usually sufficient framework. However, the incorporation of own packages into ROOT is sometimes quite problematic. Therefore the RootCore [42] has been developed as light-weight framework connecting the ROOT and frequently used Athena packages into more user-friendly environment.

The RootCore is package system, which contains only basic shell scripts for the package management. It uses SVN system for version management and GNU make files [44] for compilation management. The RootCore also supports the simple package dependency, which is defined inside make file. Recently it is usable only for linux-like operating system. Best advantage of RootCore is that is not needed to load whole Athena to be able to use one or few package. Moreover the RootCore is implemented on GRID nodes.

---

[2] The loose quality in this case means that not every lepton identification criteria are applied. For example the isolation of leptons has been excluded.

The TopRootCore is based on RootCore framework and connects several packages which are necessary to work with official `NTUP_TOP` files. The TopRootCore is developed with cooperation of whole ATLAS top physics group. The general package is TopRootCoreRelease (TRCR), which contains list of packages and the shell script for installation.

Since the corrections on jet energy scale and jet energy resolution needs to be applied on data, several packages are implemented to provide these correction. Furthermore there are packages for jet uncertainties calculation. The b-tagging information is accessible by MV1Tagger package.

Apart from jets the muons efficiency and momentum correction is incorporated into TopRootCore. Similar corrections are applied for electrons. Moreover for misidentified photons finding there is PhotonIDTool package.

As was mentioned before, the detector conditions are changing during the year and also during the run. Therefore the database of physically relevant events is created. The GoodRunLists package provides access to this database and connect it with data. Also packages for trigger menu, bunch-crossing and pile-up reweigting tools are components of TopRootCore.

The D3PD file type (see Sec. 3.1.2) is accessible by TopD3PDAnalysis package, which calls methods from other packages providing selection, corrections, scale-factors etc.

Our mini-ntuples are different from official and therefore it was needed to create code producing this mini-ntuple structure. For this purposes the TopDilAna [45] package has been added to TopRootCore (version TRCR11-00-00-05). This package provides selection of events and it creates mini-ntuples with all official corrections applied.

Events in the mini-ntuples are stored in TTree structure containing branches with all necessary information for our analysis like kinematic values of leptons and jets (p_x,p_y,p_z,E), missing transversal momentum (magnitude and direction). Also detector-related information (LAr error flag), event identification (run number, event number, lumi-block number etc.), b-tagging weights and others are included. In case of Monte Carlo samples there is additional TTree with true kinematic values of generated particles and run number/event number to be able to pair the events.

The last but not least procedure with mini-ntuples is kinematic reconstruction of $t\bar{t}$ system. The kinematic reconstruction could be accomplished by several methods. The method used in our case is simple solution of set of non-linear kinematic equations (explained later in Sec. 4.3). The numerical solution is performed by Newton-Raphson method [46]. The code has been successfully used for estimation of W boson helicity fractions at CDF experiment. The reconstructed values are added into TTree as new branches and the final size of the mini-ntuple is 0.3 kB/event, which could be comfortably used on personal computer.

CHAPTER 4

MEASUREMENT OF CHARGE ASYMMETRY

In this chapter are presented the ingredients needed for the measurement of charge asymmetry: selection of events, modeling of signal and background processes and kinematic reconstruction of $t\bar{t}$ system. The analysis objects are leptons, jets from b quarks and missing transversal momentum from neutrinos. The measurement is performed in three dilepton sub-channels ee, $e\mu$ and $\mu\mu$.

There are results [47] from measurement of charge asymmetry of top quarks pair production in dilepton channel by ATLAS experiment. However, the resulted distribution has not been unfolded and different method has been used for the reconstruction of the $t\bar{t}$ system.

4.1 Event selection

As it has been described in chapter 2 the electrons in ATLAS are detected [48] as electromagnetic showers in LAr calorimeter. The clustering of showers is done by sliding window technique. Then it is searched for track from inner detector which matches the cluster after extrapolation to the calorimeter middle layer.

Muons are triggered by RPC and TGC and the regions of interests are provided for reconstructing algorithm. The combined muon reconstruction technique has been used. It means that tracks from muon spectrometer and inner detector are matched by χ^2-test. The energy loss and detector geometry is taken into account during extrapolation of tracks.

Furthermore electrons and muons need to be well isolated, i.e. there is no additional jet in spatial angle $\Delta R = 0.3$ around the incident lepton.

Jets are triggered as isolated energy clusters found by sliding window algorithm. The reconstruction of jets is time-consuming operation, due to fact that anti-k_t algorithm [49] is used with cone parameter $R = 0.4$. The jet energy scale and jet energy resolution and other correction factors has been obtained from data–MC comparison [50] and has been applied to our sample.

The missing transverse momentum is at trigger level counted from calorimeter only. After reconstruction of all physical objects and application of all corrections the missing transverse momentum can be calculated more precisely. Beside the magnitude, the direction of missing transverse momentum is reconstructed as well.

The analysed data corresponds to integrated luminosity $4.7\,\mathrm{fb}^{-1}$ from LHC proton-proton collisions recorded by ATLAS detector in year 2011.

The criteria on electron and muon triggers has slightly changed during the year 2011. Apart from that initial EF trigger for our analysis has required electron with $E_T > 20-22$ GeV and muon $p_{\mathrm{T}} > 18$ GeV. Furthermore the primary vertex has to have at least four tracks and cosmic muon rejection were applied.

There have to be at least two leptons as well as no inappropriate jet has to be in the event. The ee and $\mu\mu$ channel triggered events which should overlap with $e\mu$ channel has been removed. The cuts on missing transversal energy $E_{\mathrm{T}}^{\mathrm{miss}} > 60\,\mathrm{GeV}$ (for ee and $\mu\mu$) or on scalar sum of the leptons and jets transversal momentum $H_T > 130$ GeV (for $e\mu$) has been applied. In addition each event has to contain at least two jets.

The ee channel specific criteria is that event has to contain exactly two electrons, similar condition for $\mu\mu$ channel are two muons and for $e\mu$ it is exactly one electron and one muon.

Moreover common condition for all channels is that events have to contain leptons with opposite electric charge. Besides the invariant mass of ee and $\mu\mu$ system $m_{\ell\ell} > 15$ GeV and $|m_{\ell\ell} - m_W| > 10$ GeV, where m_W is PDG value of W boson invariant mass.

Last but not least there has to be no suspicion to malfunction of LAr calorimeter, which means that LAr-error-flags from Data Quality database must be zero in the all selected events.

4.2 Modeling of signal and background

The $t\bar{t}$ signal was generated using next-to-leading Monte Carlo generator MC@NLO [51]. The input parameters like top mass $m_t = 172.5$ GeV, W-boson mass $m_W = 80.399$ GeV and its width $\Gamma_W = 2.085$ GeV^{-1} has been determined according to [52]. Moreover the CT10 [53] parton density functions have been used with tunning AUET2-CT10 [54]. In addition the parton showering and underlying event has been modeled by HERWIG [55] and JIMMY [56] generators.

For the purpose of normalization the cross-section $\sigma_{t\bar{t}} = 166.78^{+16.48}_{-17.76}\,\mathrm{pb}$ has been calculated by HATHOR [11] – the $t\bar{t}$ production cross-section calculation program, which uses the corrections up to NNLO.

Also background process events has been simulated by Monte Carlo generators to obtain overall background contribution.

The single top electroweak production has been simulated by MC@NLO and AcerMC [57] generators. The event containing W and Z bosons with jet associative production has been generated by ALPGEN [58] with HERWIG and JIMMY parton showering and underlying event generators. Furthermore the diboson (WW,WZ,ZZ) production modeling has been provided by HERWIG.

Also pile-up corrections has been included into generated events. Moreover all distributions has been reweighted according to measured distribution of interaction multiplications per bunch-crossing.

Since there are physical processes which could produced fake high-p_T electrons or muons, the rate of such processes needs to be evaluated. The fake muons could origin for example from long lived hadrons like K and $\pi^{\pm}$ or semi-leptonic b decays. The misidentified π^0 shower, electrons from photon conversion and direct photons are some of the contributions to the fake electrons. The simulation of such events is hard. Therefore data are used to estimated such “fake” events using matrix method, which uses “loose” and “tight” category of leptons.

from measured $Z \to \ell\ell$ sample, are selected with tight and loose cuts. Afterwards the rate of the fake leptons is estimated from ratios between numbers of the tight and loose leptons.

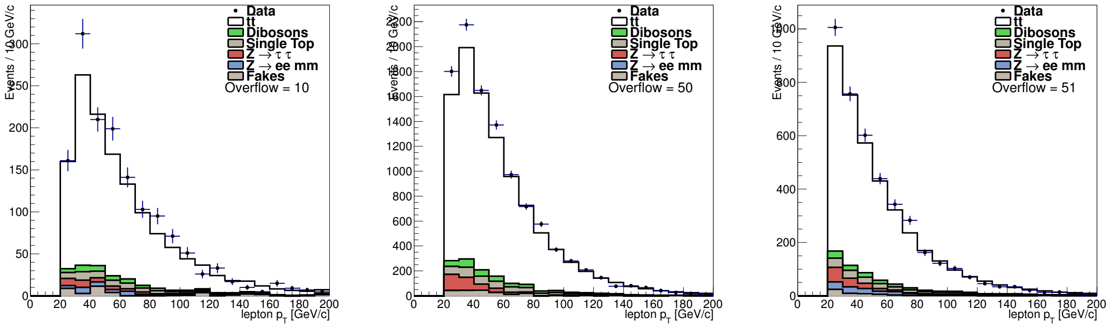

(a) ee channel (b) $e\mu$ channel (c) $\mu\mu$ channel

Figure 4.1: Expected and measured distribution of transversal momentum of leptons (and anti-leptons).

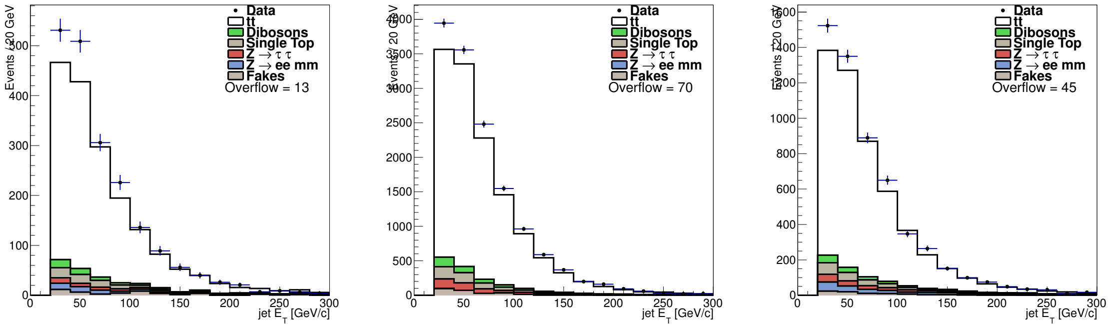

(a) ee channel (b) $e\mu$ channel (c) $\mu\mu$ channel

Figure 4.2: Expected and measured distribution of transversal energy of jets.

To conclude data selection and modeling, the Tab. 4.1 with observed number of events is compared to signal and background expectations are presented. The statistical uncertainties in table has been estimated from size of the sample. If we take into account 10% of systematic uncertainty of $t\bar{t}$ cross-section, the measured data are well compatible with the predictions.

The expected and measured distributions of lepton transversal momentum, jet transversal energy and jet multiplicity are shown on Fig. 4.1, Fig. 4.2 and Fig. 4.3 respectively.

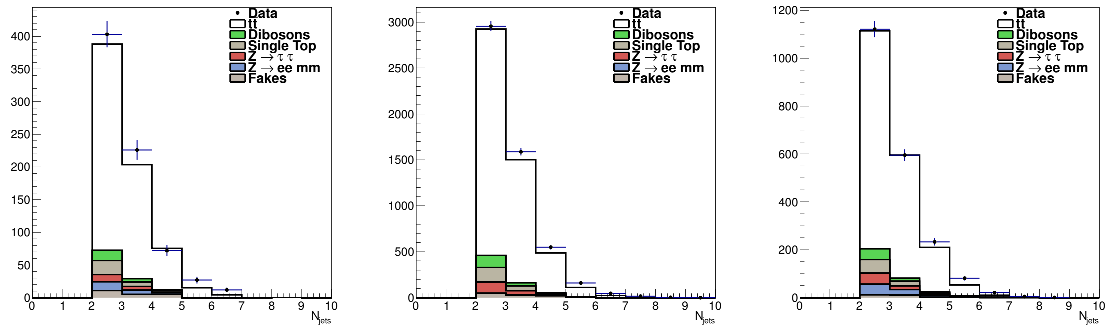

(a) *ee* channel (b) $e\mu$ channel (c) $\mu\mu$ channel

Figure 4.3: Expected and measured distribution of jet multiplicity.

Channel	ee	$e\mu$	$\mu\mu$
$t\bar{t}$	573 ± 5	4368 ± 15	1665 ± 9
Dibosons	23 ± 1	177 ± 3	61 ± 2
Single top	31 ± 2	228 ± 5	84 ± 3
$Z \to \tau\tau$	18 ± 2	180 ± 6	68 ± 4
$Z \to ee/\mu\mu$	23 ± 2	2 ± 0	80 ± 4
Fakes	19 ± 8	97 ± 15	28 ± 3
Total	690 ± 10	5050 ± 20	1990 ± 10
Data	740 ±	5320 ±	2060 ±

Table 4.1: Expected and observed numbers of events, with statistical uncertainties.

4.3 Kinematic reconstruction of $t\bar{t}$ system

Because the top quark has short lifetime it can not be measured directly, only its decay products are detected. There is more than one way how to reconstruct four-vectors of top quarks. The method, which has been used in our analysis, is based on multiple solution findings of kinematic equation system.

Owing to dilepton channel, the kinematic reconstruction objects are two leptons, two jets and missing transversal momentum. As has been written in section 1.3 both of the top quarks decay through W boson, which both decay into lepton and neutrino in our case. With respect to the flavour of leptons the measurement is divided into three channels: electron–electron ee, electron–muon $e\mu$ and muon–muon $\mu\mu$.

The system of kinematic equations could be described as

$$
\begin{aligned}
p_t &= p_{W^+} + p_b && \text{(4.1a)}\\
p_{\bar{t}} &= p_{W^-} + p_{\bar{b}} && \text{(4.1b)}\\
p_{W+} &= p_{\ell+} + p_\nu && \text{(4.1c)}\\
p_{W-} &= p_{\ell-} + p_{\bar{\nu}}\ , && \text{(4.1d)}
\end{aligned}
$$

where p are the four-momenta of particles in index. These 16 equations contains 22 unknowns: four-momenta of top quarks, $W^\pm$ and the three-momenta of neutrinos (assuming massless neutrinos). There are 16 measured quantities – four-vectors of leptons and b-quarks. To be able to solve the system, six additional conditions must be provided. These constrains are the masses of all particles are and the two additional equations from measured $E_{\mathrm{T}}^{\mathrm{miss}}$ Eq. 4.2.

$$
\begin{aligned}
p_t^2 &= p_{\bar{t}}^2 = m_t^2 && \text{(4.2a)}\\
p_{W+}^2 &= p_{W-}^2 = m_W^2 && \text{(4.2b)}\\
E_{\mathrm{T}}^{\mathrm{miss}} &= \vec{p}_{T\nu} + \vec{p}_{T\bar{\nu}} && \text{(4.2c)}
\end{aligned}
$$

where p_T is transverse momentum, invariant mass of top (anti-)quark is assumed to $m_t = 172.5$ GeV, invariant mass of $W^\pm$ bosons is $m_W = 80.4$ GeV.

The Newton-Raphson method [46] has been used for solution of non-linear system of equations. To be able to use this method the system of equations have to be in form

$$
F_i(x_1, \cdots, x_N) = 0 \qquad i = 1, 2, \cdots, N \tag{4.3}
$$

The method iteratively variates the unknowns $\boldsymbol{x}$ to find the solution with zero right hand side. The Jacobian of equations system is defined as $J_{ij} = \frac{\partial F_i}{\partial x_j}$. Consequently the step $\delta\boldsymbol{x}$ could be obtained from system of equations $\boldsymbol{J} \cdot \delta\boldsymbol{x} = -\boldsymbol{F}$. Usually it is better to limit number of iterations. The iteration equation could be written as

$$
\boldsymbol{x}_{\mathrm{new}} = \boldsymbol{x}_{\mathrm{old}} + \delta\boldsymbol{x}\ . \tag{4.4}
$$

The uncertainties of measured values have been taken into account, i.e. the reconstruction has been repeated many times (100) with randomly smeared jet momentum and $E_{\mathrm{T}}^{\mathrm{miss}}$ in order to uncertainties.

There could be more than two jets in the event. The two highest p_T jets are taken and all lepton–jet pair combination are created. The $t\bar{t}$ system is solved hundred times for each pair combination. The number of successful reconstructions is stored for each combination and the one with greater number of successful reconstructions is chosen as final.

Chapter 5

Unfolding studies

In this chapter some of widely-used unfolding methods in high energy physics will be introduced. Afterwards the one specific method will be chosen and the optimization of its parameters will be described.

5.1 General notes

It is common to analyse the physical phenomena independently on given experiments. In order to be able to compare the results between experiments (and theory) it is needed to extrapolate measurement to the level, which is common for all experiments. This process is called unfolding, unsmearing or deconvolution. In our case the distribution of absolute rapidity difference between top and anti-top quarks $\Delta|y_{t\bar{t}}|$ and distribution of absolute difference of opposite-charged-lepton pseudorapidity $\Delta|\eta_{\ell^+\ell^-}|$ will be unfolded to the parton (generator) level.

Little bit of definitions and terminology should be suitable for next reading (inspired by article [59]). Let observable y have values from $y_{\min}$ to $y_{\max}$ and one divides this range into ℓ disjunctive subranges called bins. If one repeatedly measures observable y then results can be stored in form of an histogram.

Histogram $\boldsymbol{m}$[1] is an ℓ-tuple of numbers $\boldsymbol{m} = (m_1, \cdots, m_\ell)$, where number m_i represents how many times the result of y measurement has been from i^{th} subrange (bin). Furthermore normalized histogram from probabilistic point of view has role of a probability distribution function of variable y. Theoretical tools of probability, definitions and relations could be found in [4] or [34] for instance.

All unfolding studies have in common the analysis of discrepancies between measured $\boldsymbol{m}$ and real physics values $\boldsymbol{n}$. These discrepancies usually originate from the detector finite resolution, the limited acceptance, background contribution etc. The starting point has been the Monte Carlo modeling of studied physics events (described in Sec. 4.2), when the "truth" (or generated) histogram $\boldsymbol{\nu}$ is obtained.

In our case, the simulation of detector response and the reconstruction[2] has been provided on generated events and reconstructed distribution $\boldsymbol{\mu}$ is obtained. The reconstruction of Monte Carlo events is identical as the reconstruction used for data. However, the measured distribution $\boldsymbol{m}$ is not equal to $\boldsymbol{\mu}$, because of the background contribution. The estimated background $\boldsymbol{\beta}$ (see Sec. 4.2)

---

[1] Here and after all bold symbols will represent ℓ-tuple ($\ell \in \mathbb{N}$) or vector.

[2] The reconstruction includes kinematic reconstruction of the $t\bar{t}$ system.

have to be subtracted from the data.

For the deconvolution it is useful to know, how the truth values have changed in process of reconstruction. In other words, what is the probability, that event, which origins from generated bin ν_j, "moves" to reconstructed bin μ_i. The response matrix $\mathcal{R}$ contains exactly this kind of information.

$$\mathcal{R}_{ij} = P(\text{observed in bin j} \mid \text{true value in bin i}) \;, \tag{5.1}$$

where $P(A|B)$ is conditional probability (see [34] for definition). The response matrix could be also represented as a 2-dimensional histogram (Fig. 5.1) with reconstructed values on x-axis and generated on y-axis. More response matrices could be found in Appendix A.

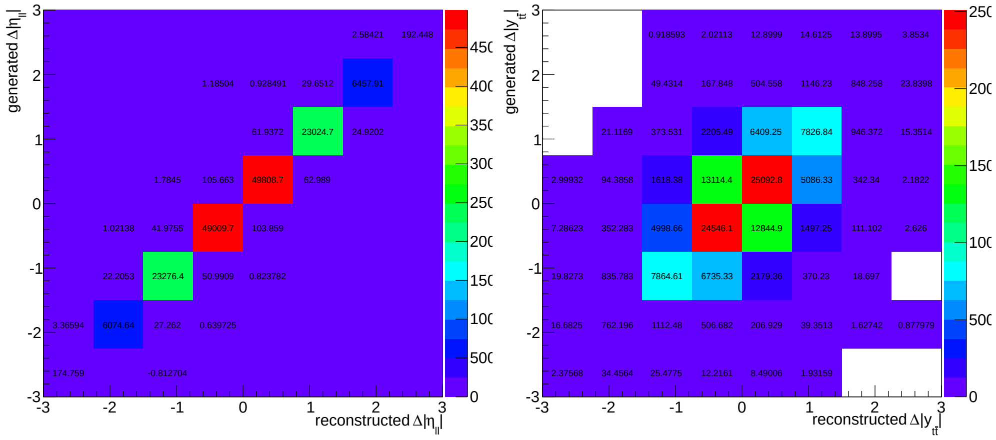

(a) Lepton response matrix

(b) Top response matrix

Figure 5.1: The example of used response matrices, showed as 2-dimensional histograms. The distribution represent number of events in generated vs. reconstructed distributions. More description in text.

Of course it is possible, that some event has not been reconstructed nor selected. Also this information is stored. Consequently the efficiencies could be calculated and applied, what is needed especially in case of deconvolution to the parton level. The process of filling response matrix and the efficiency estimation will be denoted as teaching.

The teaching must be provided for each measured quantity separately. it means that separate response matrices for $\Delta|y_{t\bar{t}}|$ and $\Delta|\eta_{\ell^+\ell^-}|$ and also for each channel has been created. Owing to fact that not every method is capable of processing different number of bins in generated and reconstructed distributions, during studies it has been created matrices per each studied number of bins.

Generally the process of unfolding U could be written as

$$\hat{\boldsymbol{m}} = U(\boldsymbol{m};\boldsymbol{\beta},\boldsymbol{\theta}) \ , \tag{5.2}$$

where $\boldsymbol{m}$ is distribution observed in data, $\boldsymbol{\beta}$ is expected contribution of background, $\boldsymbol{\theta}$ are parameters of unfolding and $\hat{\boldsymbol{m}}$ is unfolded distribution, which should be equal to real physics distribution $\boldsymbol{n}$. The main goal of unfolding is finding the right function U and its parameters. Moreover different methods provide different prescription of this function, but usually the function has matrix form and it uses information from response matrix. After choosing of method the suitable parameters $\boldsymbol{\theta}$ have to be estimated (e.g. regularization parameter, number of iterations etc.). The expected background is usually subtracted from measured data and therefore the input to unfolding is signal-only distribution.

The unfolding methods could be implemented into ROOT by the RooUnfold package [52]. The RooUnfold package contains tool for creating the response matrices (also multidimensional) RooUnfoldResponse. Besides that this class provides basic filling of response matrix it also stores information about truth and measured distributions. This is performed by method Miss, which stores information about the events which has not been reconstructed nor selected. Also the Fakes method is available for background subtraction, but we have not used it.

Every unfolding method has own class, where the all needed numerical algorithms are specified. There are also the calculations of method uncertainties. All deconvolution classes are derived from abstract class RooUnfold. This allows us simply test the different methods between each other.

The main code of our unfolding analysis TopDilUnf [60] has been written as RootCore package. Inside the TopDilUnf one can find all algorithms used to produce results discussed in this chapter. The TopDilUnf uses ROOT tools with RooUnfold classes to provide unfolding.

5.2 Deconvolution methods

If the measured distribution of observable y is described by well known relation or space of functions $\Upsilon(y,\boldsymbol{\theta})$ of real physics values, it is simple to find the real values from measured distribution. In such case it is sufficient to find (fit) the parameters $\boldsymbol{\theta}$ of measured values y and correct the distribution against reconstruction effects. Unfortunately, the space of function in our measurement is wide-ranging and not well-known. Consequently it has been needed to use method based on theory of probability and statistics.

5.2.1 Bin-by-bin method

By simple comparison of generated and reconstructed spectrum it is possible to estimate efficiencies for each bin separately. This is how method of correction factors (or bin-by-bin) treats problem of deconvolution. The formula of bin-by-bin unfolding is

$$\hat{m}_i = C_i \cdot (m_i - \beta_i) \ , \tag{5.3}$$

where the histograms are defined same as above Eq. 5.2 and C_i are correction factors related to efficiencies. Each bin of measured distribution (subtracted by background) is simply multiplied by correction factor C_i obtained from Monte Carlo simulation

$$C_i = \frac{\nu_i}{\mu_i} \tag{5.4}$$

where ν_i and μ_i are i^{th} bin contents of generated and reconstructed distributions respectively.

The bias of this method is strongly dependent on these correction factors and therefore it is important to have as much correct model as possible. If one looks more deeply at this method one finds out that it not uses full information stored in response matrices. Therefore it has been more appropriate to look at some methods, which benefit from all response matrix elements.

5.2.2 Response matrix inversion

The main task of unfolding is to describe how to change measured distribution to obtain truth values. As was written above the response matrix $\mathcal{R}$ contains information how the truth distribution $\boldsymbol{\nu}$ has been changed to reconstructed distribution $\boldsymbol{\mu}$.

$$\mathcal{R}\boldsymbol{\nu} = \boldsymbol{\mu} \tag{5.5}$$

Finding solution of the response equation Eq. 5.5 is the basic problem of unfolding and the methods differs according to how do they solve this problem. As name of this subsection says this method is based on inverting the response matrix $\mathcal{R}$. Consequently, first necessary condition for using this method is that the response matrix is invertible. This solution is more or less numerical problem, which has been studied for example in [46]. Mathematical expression of the unfolding is therefore

$$\hat{\boldsymbol{m}} = \mathcal{R}^{-1} \cdot (\boldsymbol{m} - \boldsymbol{\beta}) \tag{5.6}$$

where inverted response matrix $\mathcal{R}^{-1}$ is simply multiplied by measured distribution subtracted by estimated background contribution $(\boldsymbol{m} - \boldsymbol{\beta})$.

This method has not been used, because of the fact, that if there are large numbers in non-diagonal elements (e.g. Fig. 5.1b), the method has very large uncertainty. It has been needed to use methods, which are less sensitive to non-diagonal elements.

5.2.3 Singular value decomposition

This method is very similar to matrix inversion. But before solving the response equation (Eq. 5.5) the factorization of response matrix is provided to the form

$$\mathcal{R} = USV^T \ . \tag{5.7}$$

This factorization is called singular value decomposition (SVD) and matrices U and V are both orthogonal, i.e. $UU^T = U^TU = I$, where I is unitary matrix and symbol "T" denotes transposed matrix. Matrix S is defined as $S_{ij} = 0$ for $i \neq j$ and $S_{ii} = s_i \geq 0$. This system could be solved much more easier than response matrix inversion and despite the inversion, this method could be also used in case of different binning in generated and reconstructed distribution.

The SVD unfolding could be simply written

$$\hat{\boldsymbol{m}} = VS^{-1}U^T \cdot (\boldsymbol{m} - \boldsymbol{\beta}) \ , \tag{5.8}$$

where it is needed to transpose matrices U and V^T from Eq. 5.7 and find inverse matrix to S, which is diagonal and therefore it is more effective than response matrix inversion. The disadvantage of this method is that it can not be extended to multidimensional distributions, which will be needed in the next step of our analysis.

5.2.4 Iterative D'Agostini method

The Bayes theorem is one of the basic relations of probability. The theorem represents the relation of conditional probabilities $P(A|B)$

$$P(A|B) = \frac{P(B|A)P(A)}{P(B)} \ . \tag{5.9}$$

The theorem is frequently used for testing the hypothesis of measurement results and in 1995 the iterative unfolding method based on this theorem has been developed by G. D'Agostini[3].

D'Agostini in his work [61] starts from the definition of the "cause" and "effect", which in our work corresponds to generated $\boldsymbol{\nu}$ and reconstructed $\boldsymbol{\mu}$ distributions, respectively. The unfolding procedure in matrix form will be (similar as in previous methods)

$$\hat{\boldsymbol{m}} = \boldsymbol{U} \cdot (\boldsymbol{m} - \boldsymbol{\beta}) \tag{5.10}$$

where $\boldsymbol{U}$ is unfolding matrix and $\hat{\boldsymbol{m}}$, $\boldsymbol{m}$, $\boldsymbol{\beta}$ are the unfolded, measured, background histograms respectively.

The important point is to realize that one probability, which is already known, is represented by the response matrix $\mathcal{R}_{ij} \approx P(\mu_j|\nu_i)$. And the other conditional probability is the searched unfolding matrix $U_{ij} \approx P(\nu_i|\mu_j)$. To be precise one must incorporate the efficiency of reconstruction and selection process. The efficiency ε_i of i^{th} bin is a real number defined as

$$\varepsilon_i = \frac{\sum_k \mathcal{R}_{ik}}{\nu_i} \tag{5.11}$$

---

[3] The Bayesian theorem in unfolding has also been used before D'Agostini iterative method, but the methods are not well documented.

The Bayes theorem for our case could be rewritten to obtain the unfolding matrix $\boldsymbol{U}$ as

$$U_{ij} = \frac{\nu_i}{\sum_k \mathcal{R}_{ik}} \frac{\mathcal{R}_{ij}\nu_i}{\sum_k \mathcal{R}_{ik}\nu_i} \ , \tag{5.12}$$

where the first fraction stands for inverse efficiency $\frac{1}{\varepsilon_i}$ from Eq. 5.11 and second fraction is rewritten Bayes theorem. Even though the Eq. 5.9 contains the probabilities, we can write the response matrix and histogram directly, because the normalization factors cancel out in fraction.

After unfolding, which basically means to put $\boldsymbol{U}$ from Eq. 5.12 to Eq. 5.10 and evaluate, the obtained unfolded distribution $\hat{\boldsymbol{m}}$ is somewhere between measured $\boldsymbol{m}$ and real physics distribution $\boldsymbol{n}$. Here we can reuse this method and iteratively progress towards searched distribution. The iterative process is divided into three steps

1. The starting point is to choose the distribution $\boldsymbol{\nu}^0$, which should as much as possible presents the wanted distribution $\boldsymbol{n}$
2. Now provide the calculation of unfolded distribution with chosen $\boldsymbol{\nu}^0$
$$\hat{m}_i = \frac{\nu_i^0}{\sum_k \mathcal{R}_{ik}} \frac{\mathcal{R}_{ij}\nu_i^0}{\sum_k \mathcal{R}_{ik}\nu_i^0} \tag{5.13}$$
3. Decide whether to continue or the number of iterations is enough. If it is not, then set the new $\boldsymbol{\nu}^0 = \hat{\boldsymbol{m}}_i$ and continue from point 2.

The number of iterations is the parameter of D'Agostini unfolding and the best value needs to be estimated. This will be described in following section (Sec. 5.3).

The uncertainty of this method cumulates with number of iterations. This could be interpreted by the repetitive usage of unfolding matrix and by the fact that the more significant is change of $\boldsymbol{\nu}^0$ between following iterations the higher is increase of uncertainty.

5.2.5 Comparison of the unfolding methods

At the end of this section we will compare the results from different unfolding methods. On Fig. 5.2 there is the same $\Delta|y_{t\bar{t}}|$ distribution unfolded by different methods. As initial sample has been used the MC@NLO generator officially produced $\sim$ 15 million-event ntuple. The selection criteria (described in Sec. 4.1) have been used and selected events has been reconstructed by method described in Sec. 4.3.

The teaching sample for response matrix is the same as the test, therefore Fig. 5.2 shows that the methods could be used for unfolding of the measurement, which is consistent with MC@NLO predictions. But the measured distribution should not be the same and therefore the additional analysis is needed.

The main reason why it has been decided to use the iterative D'Agostini method for unfolding of the absolute rapidity distribution difference between top quark and anti-top quark is that this

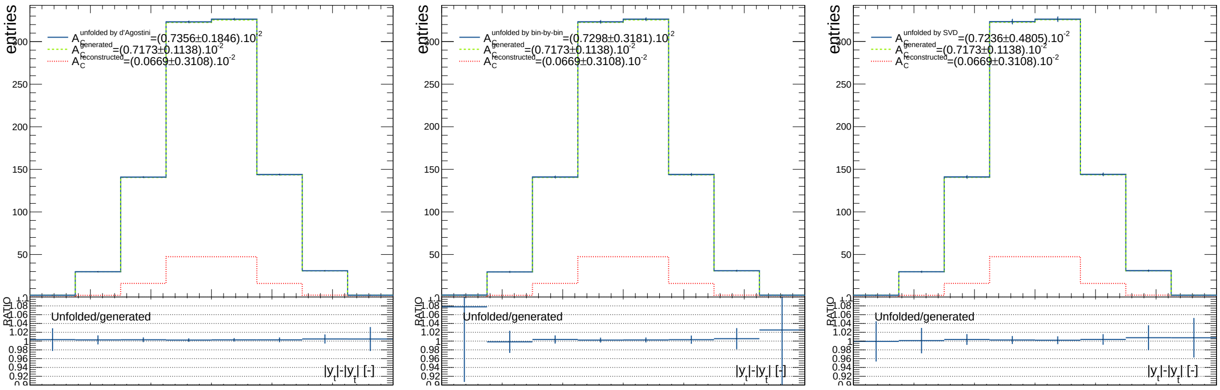

(a) unfolded by d'Agostini (b) unfolded by bin-by-bin (c) unfolded by SVD

Figure 5.2: The unfolding method comparison. The distribution of $\Delta|y_{t\bar{t}}|$ has been unfolded and on each sub-figure is used different method. For more description see text.

method is easily extendible to multiple dimensions. This will be needed in the next step of analysis, because top charge asymmetry is dependent on kinematic region of the $t\bar{t}$ system (e.g. $\Delta|y_{t\bar{t}}|$ vs. $m_{t\bar{t}}$).

5.3 Bayesian method optimization

As has been written in previous section the method which has been chosen for unfolding is iterative D'Agostini method. This method has two basic parameters: number of bins and number of iterations.

For test of both parameters has been used offcial $t\bar{t}$ Monte Carlo sample (generator MC@NLO see Sec. 4.2), which has prediction of asymmetry $\sim 0.5\%$. In order to obtain samples with different asymmetries, the re-weighting of the above mentioned Monte Carlo sample has been provided. The weights were derived from axigluon model predictions and the ratio between SM and axigluon model has been calculated. Obtained distributions are on Fig. 5.3 and there are three modeled asymmetries. The new weight w of event has been calculated by

$$w \equiv s_f \cdot n(\Delta|y_{t\bar{t}}|)\ , \tag{5.14}$$

where the s_f is Monte Carlo scale factor[4] and $n(\Delta|y_{t\bar{t}}|)$ is the content of the bin with $\Delta|y_{t\bar{t}}|$ equal to the event value. In order to obtain samples with the negative asymmetry the negative value of event $\Delta|y_{t\bar{t}}|$ has been used, i.e. $n(-\Delta|y_{t\bar{t}}|)$.

The normalization of reweighting distributions has been done by different generator from which we used. This means that reweighted distribution will not have exactly 2%, 4% or 6% value of generated asymmetry, but slightly different.

---

[4] The Monte Carlo event scale factor includes all

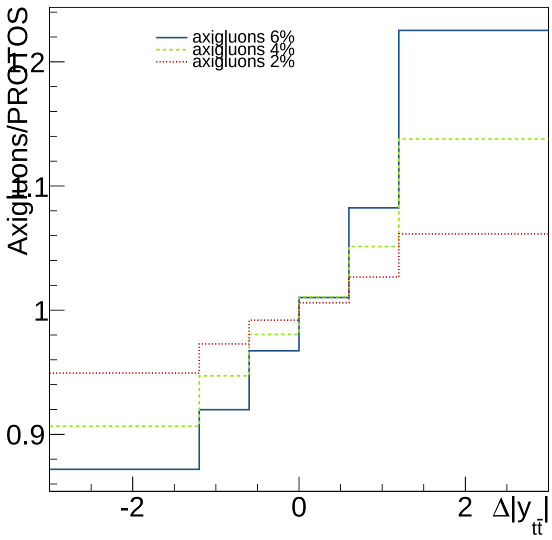

Figure 5.3: The histogram of ratio between Standard Model (PROTOS generator) and Axigluon with respect to the event absolute rapidity difference between top and anti-top quark. There are three models marked with red green and blue color representing 2%, 4% and 6% asymmetry respectively.

5.3.1 Asymmetry and number of iterations

We will see that asymmetry is more or less stabilized after few number of iterations. This plateau could be used for estimation of number of iterations. Due to that fact two conditions has been suggested.

- the relative stopping condition:

$$\left| \frac{A_C^{[i-1]} - A_C^{[i]}}{A_C^{[i-1]}} \right| \leq 1 \cdot 10^{-3} \; , \tag{5.15}$$

- the absolute stopping condition:

$$|A_C^{[i-1]} - A_C^{[i]}| \leq 5 \cdot 10^{-4} \; , \tag{5.16}$$

where for both conditions the $A_C^{[i]}$ is value of unfolded charge asymmetry after i^{th}iteration. In the other words, when the change of asymmetry according to previous iteration is sufficiently small, we found plateau and it is not needed to continue with iterations.

First it is appropriate to test the functionality of the method. The simplest possible way is to unfold the same sample, which has been used for teaching. This is shown on Fig. 5.4, where the charge asymmetry is plotted with respect to the number of unfolding iteration for both lepton and top distribution.

On Fig. 5.5 there are special points colored with orange and blue. Both points symbolize the number of iterations (in legend) which has been needed to fulfil the relative stopping condition (blue)

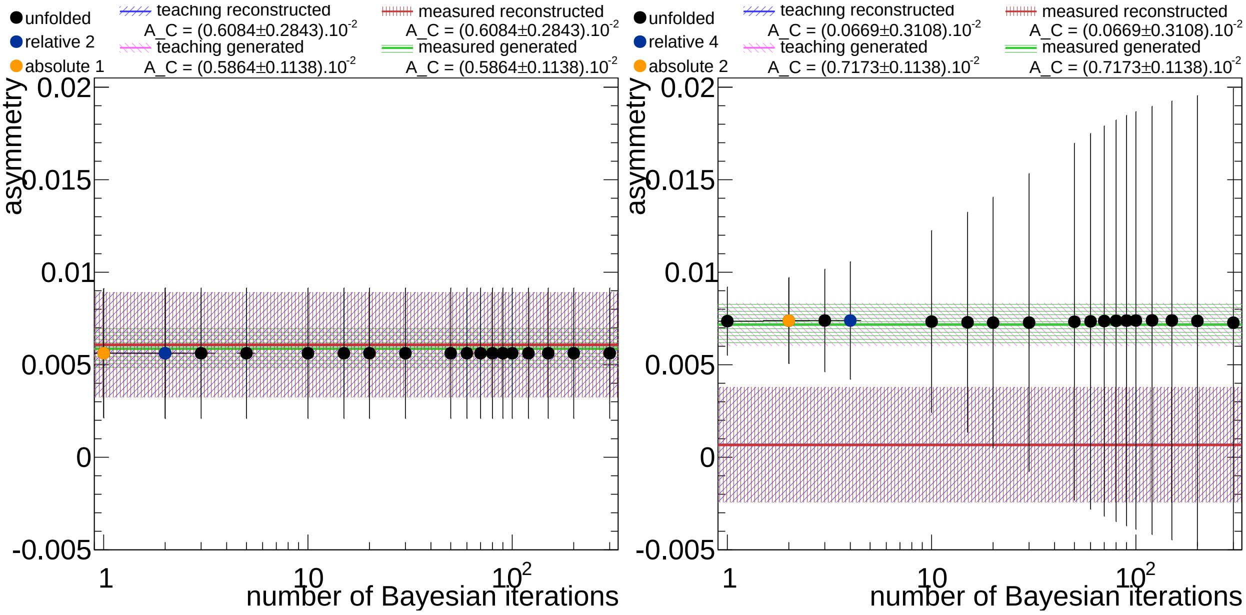

(a) Sanity check of lepton distribution $\Delta|\eta_{\ell^+\ell^-}|$.

(b) Sanity check of top distribution $\Delta|y_{t\bar{t}}|$.

Figure 5.4: Evolution of asymmetry vs. iterations. The black point shows the unfolded value of charge asymmetry with respect to the number of iterations. The blue and orange point symbolize the number of iteration needed to fulfil the absolute and relative condition respectively. The teaching sample and sample which has been unfolded (denoted as measured) are identical and therefore overlaid.

or absolute stopping condition (orange). The value of unfolded asymmetry is stabilized after few iterations near the value of generated asymmetry which is different (reweighted) for each sub-figure. The labels under sub-figures correspond to asymmetry of axigluon distribution used for reweighting.

All mentioned tests has been done on $\Delta|y_{t\bar{t}}|$ distribution with 8 bins. Furthermore, the analysis has been performed on distribution with 2, 4, 6, 8, and 40 bins. On Fig. 5.6 can be seen the unfolded asymmetry evolution with respect to number of iterations. The teaching sample is the same as measured sample, which has been unfolded, (similar to Fig. 5.4) and the distribution has 40 bins. This dependence has not stabilized even for this simple case and therefore we can exclude many-bins distribution from our next analysis. In case of 2-bins distribution is the unfolding needless. Other studied distribution (4, 6, 8 bins) has similar results. As a result the distribution with 8 bins has been chosen for next procedures.

5.3.2 Pseudo-experiments

Previous test has been done on sample much larger than measured data sample. It is important to test the unfolding on sample of same size as data sample. Therefore small sub-samples are created from full MC sample. We performed pseudo-experiments (PE), where the value is randomly picked from modeled distribution as many times as number of data events in each channel.

The PE has been created for each channel separately and also for all channels together. The

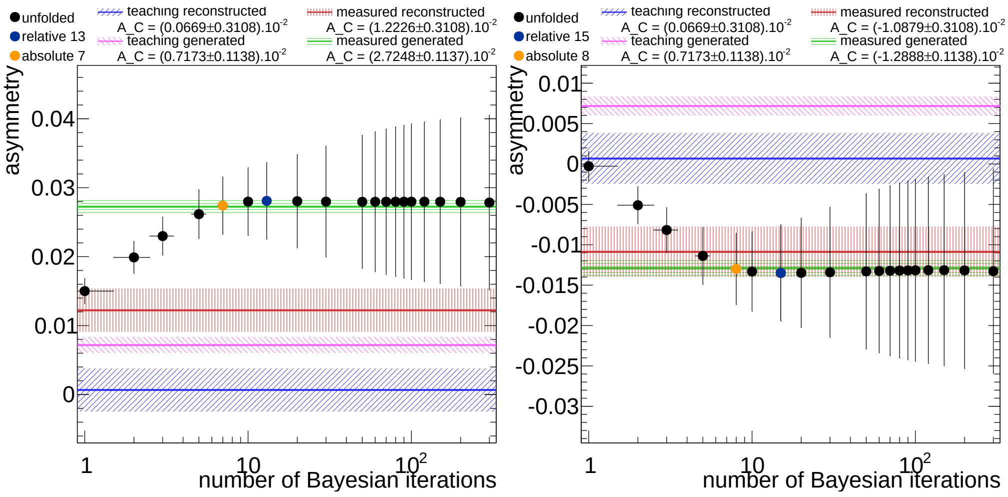

(a) Reweighted to +2%. (b) Reweighted to −2%.

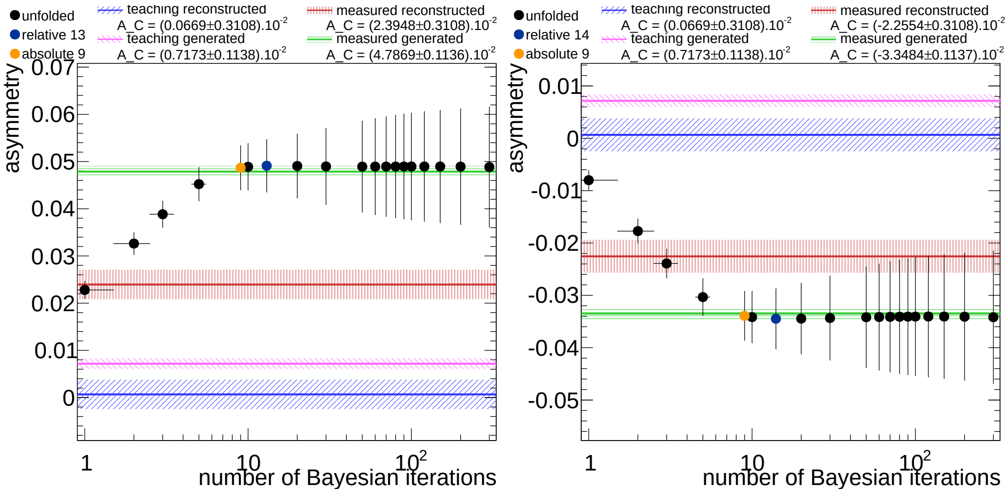

(c) Reweighted to +4%. (d) Reweighted to −4%.

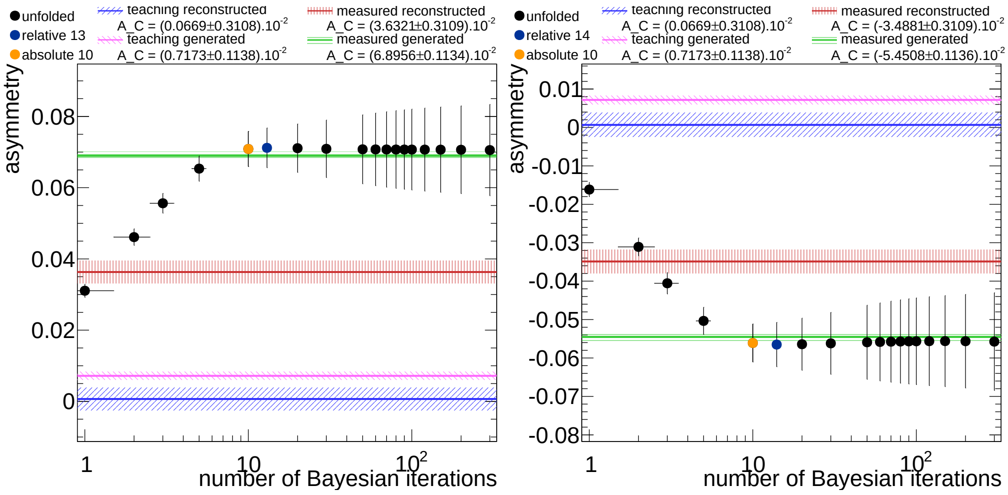

(e) Reweighted to +6%. (f) Reweighted to −6%.

Figure 5.5: Evolution of asymmetry vs. number of iterations. The black point shows the unfolded value of charge asymmetry with respect to the number of iterations. The blue and orange point symbolize the number of iteration needed to fulfil the absolute and relative condition respectively. The teaching sample is full MC and sample which has been unfolded (denoted as measured) has been reweighted by axigluon model.

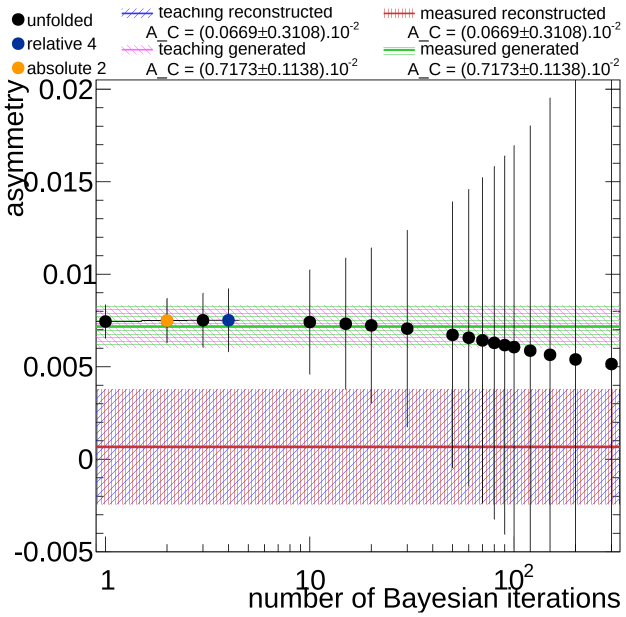

Figure 5.6: Evolution of unfolded asymmetry from distribution with 40 bins vs. number of iterations . The black point shows the unfolded value of charge asymmetry with respect to the number of iterations. The blue and orange point symbolize the number of iteration needed to fulfil the absolute and relative condition respectively. The teaching sample and sample which has been unfolded (denoted as measured) are identical and therefore overlaid.

rewieghted and original reconstructed MC distributions have been used as input for PE and also the binning studies has been performed.

If want to have statistically independent samples the number of the PE is limited by the number of events in Monte Carlo sample. Number independent PE is naturally $N_{\rm PE}^{\rm indep} = \frac{N_{\rm evt}^{\rm MC}}{N_{\rm evt}^{\rm Data}}$, where $N_{\rm evt}^{\rm MC}$ is number of events in Monte Carlo sample and $N_{\rm evt}^{\rm Data}$ is number of events in observed in data. However for certain distribution one can do more than $N_{\rm PE}^{\rm indep}$ pseudo-experiments and still uncorrelated results are obtained. The new limiting number of sub-samples is equal to $N_{\rm PE}^{\rm max} = (N_{\rm PE}^{\rm indep})^2$ according to [62]. Therefore the number of pseudo-experiments has been estimated to be 100 to fulfil new limit of quasi-independent sample.

Each pseudo-experiment distribution (for each bin, each weight, each channel) of absolute rapidity difference between top and anti-top and absolute difference between lepton pseudoprapidity has been unfolded. The number of iteration has been fixed to several values and also the study with stopping condition defined in Eq. 5.16 has been done. The distribution of iterations numbers needed for fulfil the condition in pseudo-experiments is plotted on Fig. 5.7

The stored numbers from each pseudo-experiment are: value of measured asymmetry in PE $A^{\rm init}$, value of unfolded asymmetry $A^{\rm unf}$ per each iteration, the unfolding uncertainty $E^{\rm unf}$ per each number of iterations, the number of iterations needed to fulfil the stopping condition and the pull defined as

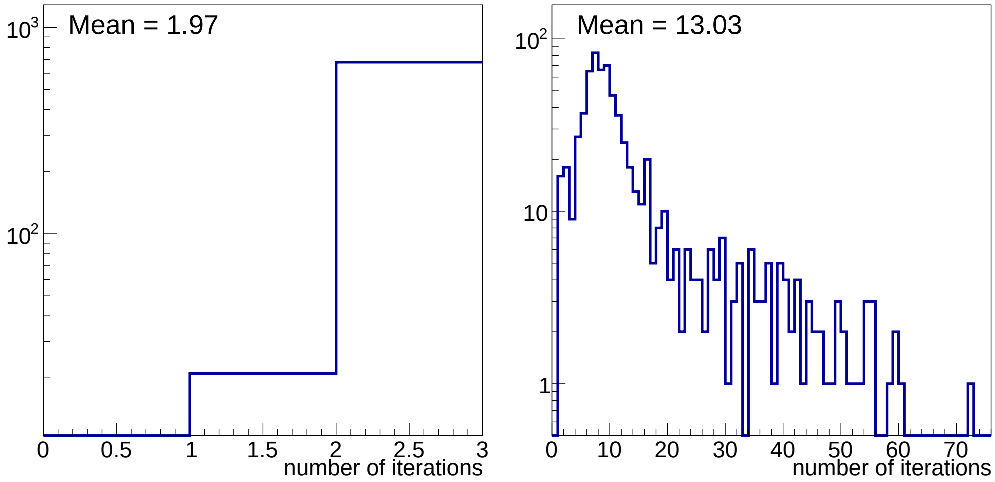

(a) Lepton pseudoexperiments.

(b) Top pseudoexperiments.

Figure 5.7: The number of iterations in pseudo-experiments needed to fulfil the absolute stopping condition Eq. 5.16 in hundred pseudo-experiments, all channels and all reweighted 8-bin distributions together.

$$P \equiv \frac{A^{\mathrm{unf}} - A^{\mathrm{gene}}}{E^{\mathrm{unf}}}, \tag{5.17}$$

where A^{gene} is value of generated asymmetry of MC sample from which the pseudo-experiment has been produced. The example of distributions are on Fig. 5.8, where the black lines represent fit with Gaussian. The fitted parameters are used in the next analysis.

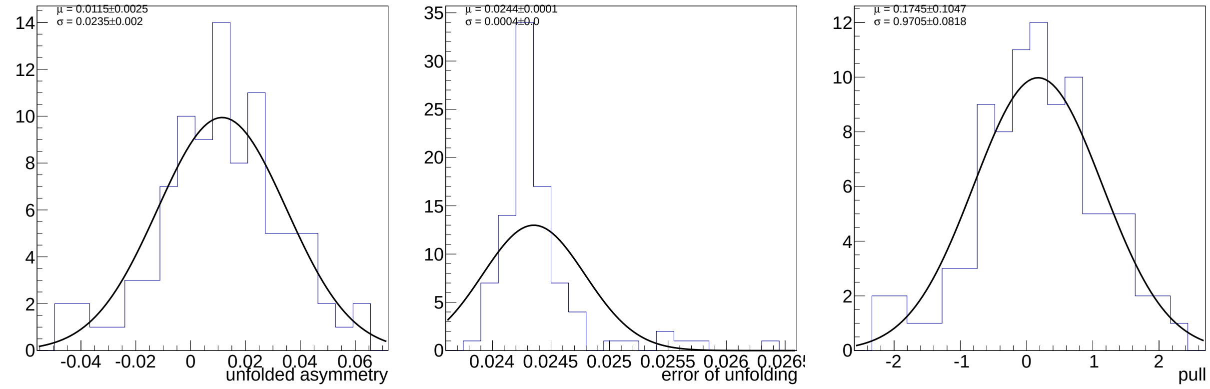

(a) Distribution of unfolded asymmetry

(b) Distribution of unfolded asymmetry uncertainty

(c) Distribution of pull

Figure 5.8: The example of distributions obtained from hundred top pseudo-experiments. The sub-figures correspond to case of 10 unfolding iterations, the initial distribution with 8 bins created from non-reweighted sample. Distribution is fitted with Gaussian and fitted parameters are in legend.

If we want to have unbiased unfolding the mean value of pull distribution have to be zero, i.e. $< P >= 0$. This is equal to situation, when mean value of unfolded asymmetry distribution is equal to generated asymmetry $A^{\mathrm{gene}} =< A^{\mathrm{unf}} >$.

To find the right value of unfolding uncertainty E^{unf} it is sufficient to look at the width of pull distribution, which should be equal to one. If the error is underestimated the pull width is more than one, if the error is overestimated the pull width is less than one.

As a result we can say that the unfolding is working correctly if the pull distribution from pseudo-experiments is Normal distribution. We will search for such an operation point, where this is fulfilled.

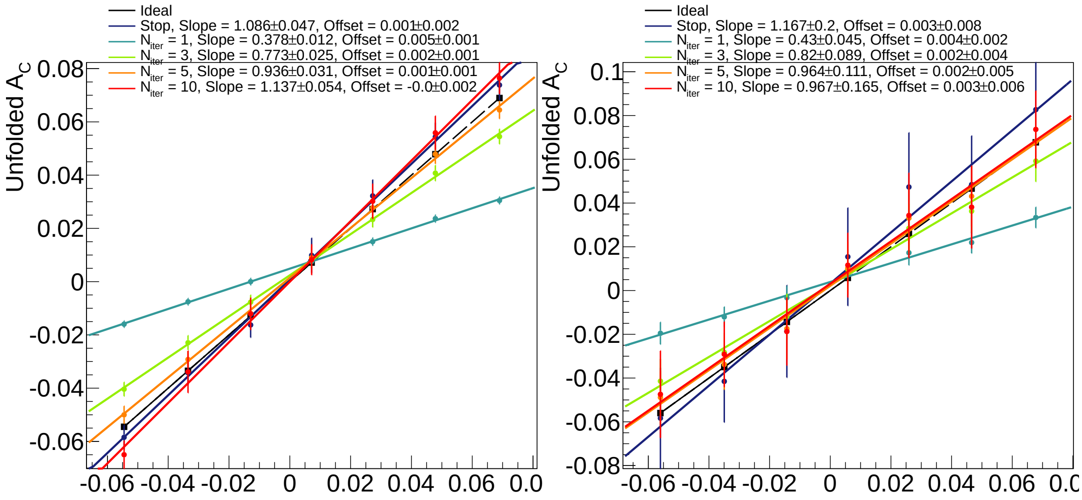

(a) All channels together.

(b) *ee* channel.

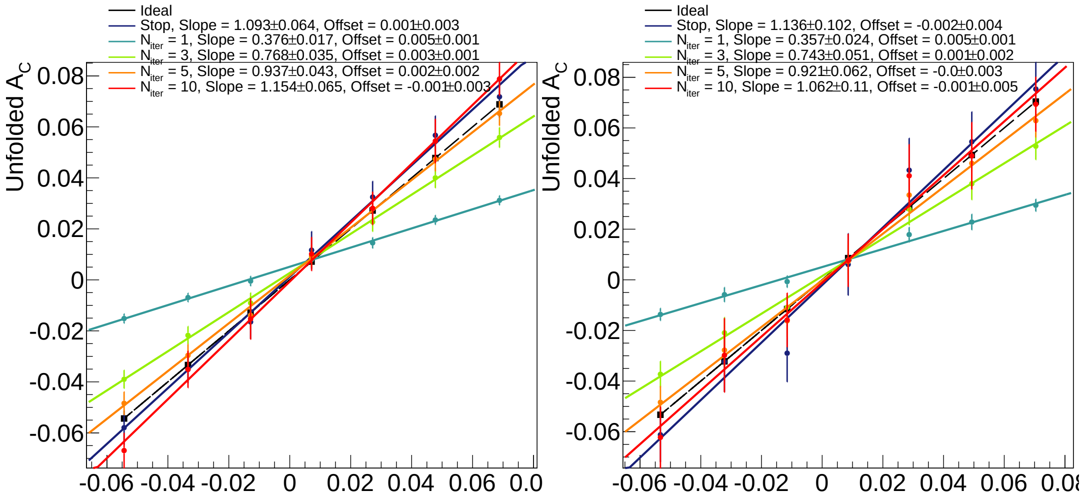

(c) $e\mu$ channel.

(d) $\mu\mu$ channel.

Figure 5.9: Mean unfolded top charge asymmetry from pseudo-experiments with respect to generated asymmetry (channel per sub-figure). The dark blue colour represents number of iterations needed to fulfil the absolute stopping condition. Other colours are unfolded by fixed number of iterations.

The fitted mean values of unfolded asymmetry distribution have been plotted on Fig. 5.9 and Fig. 5.10 with respect to corresponding generated asymmetry of pseudo-experiment. The mean

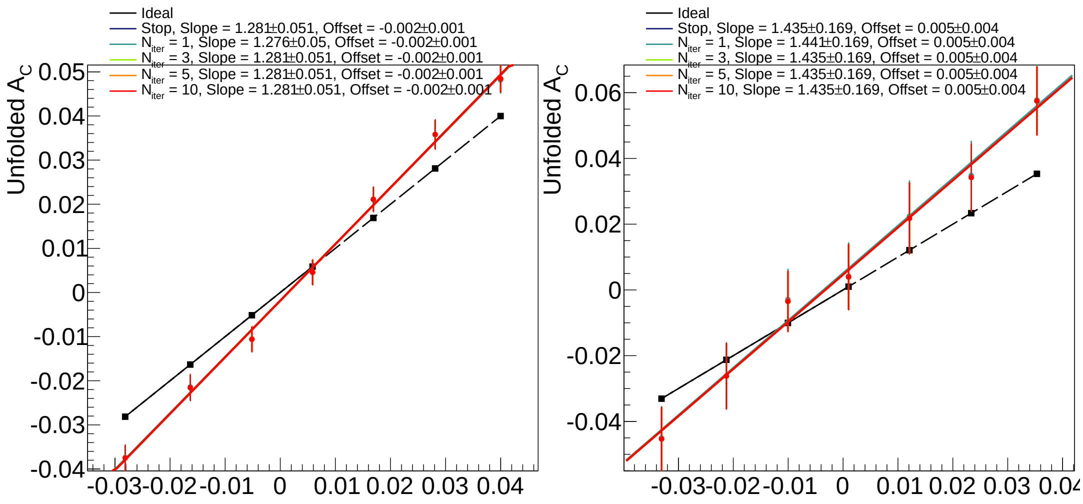

(a) All channels together.

(b) ee channel.

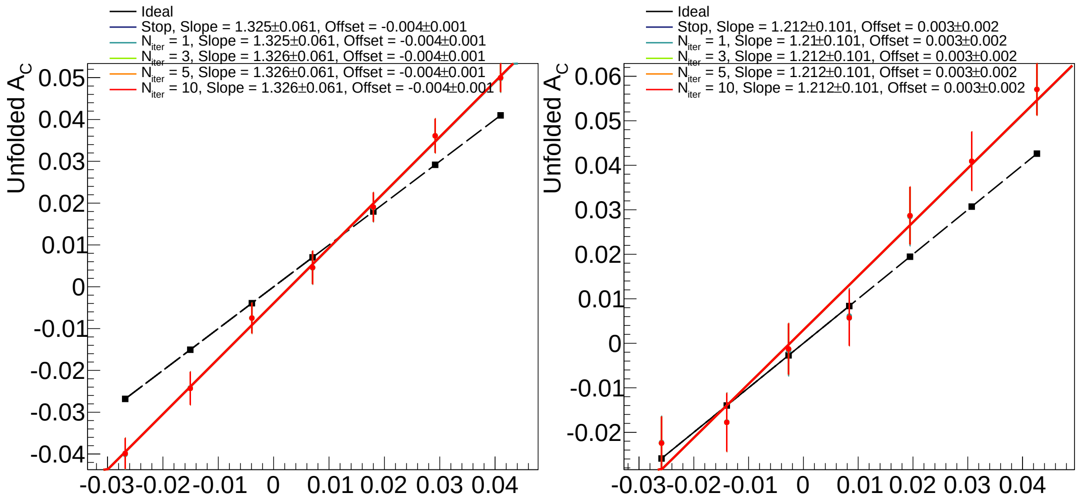

(c) $e\mu$ channel.

(d) $\mu\mu$ channel.

Figure 5.10: Mean unfolded lepton charge asymmetry from pseudo-experiments with respect to generated asymmetry (channel per sub-figure). The dark blue colour represents number of iterations needed to fulfil the absolute stopping condition. Other colours are unfolded by fixed number of iterations.

values have been evaluated for each fixed iteration (represented by colors) and also for case of fulfilling absolute stopping condition. The bias is represented by slope and offset of fitted lines.

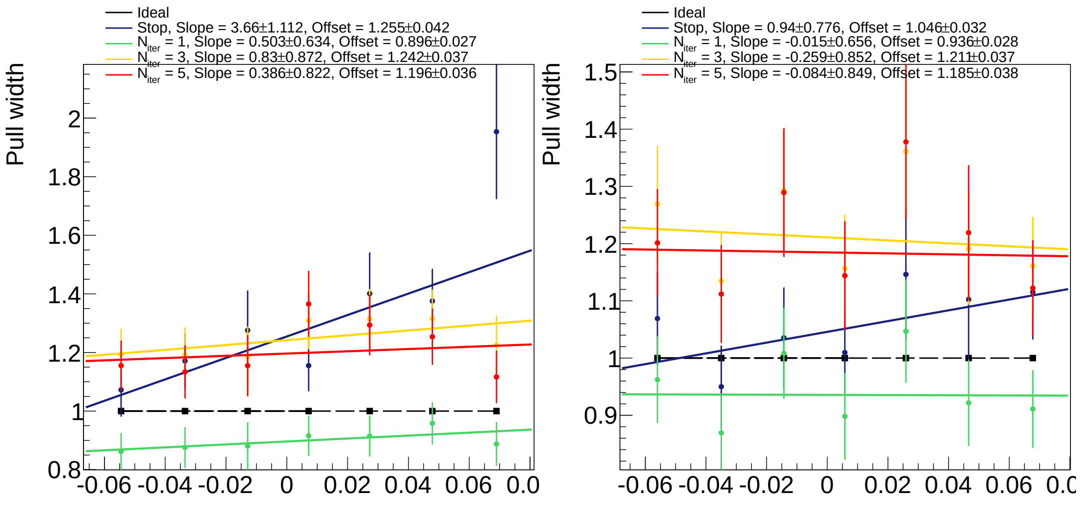

(a) All channels together.

(b) *ee* channel.

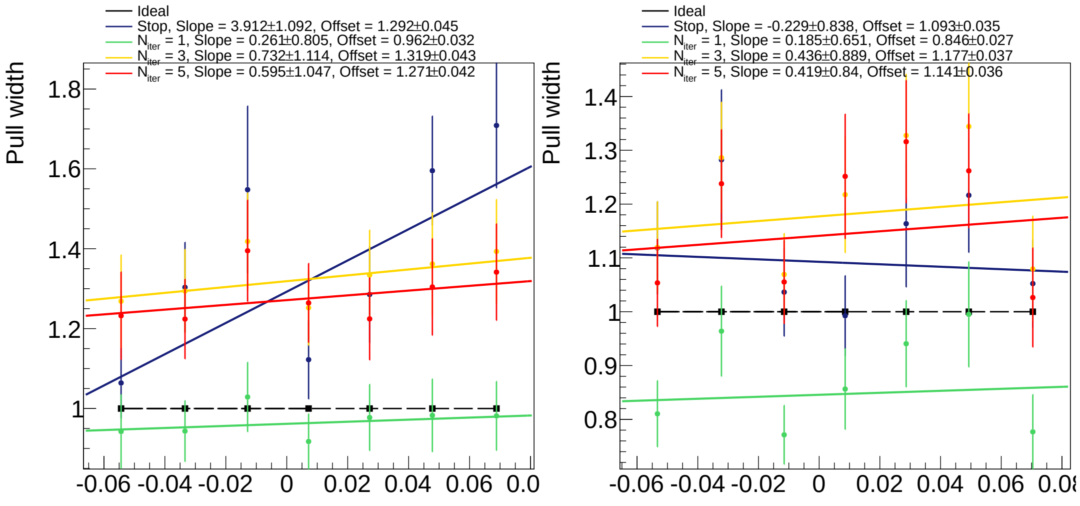

(c) $e\mu$ channel.

(d) $\mu\mu$ channel.

Figure 5.11: Top pull width with respect to generated asymmetry (channel per sub-figure). The dark blue colour represents number of iterations needed to fulfil the absolute stopping condition. Other colours are unfolded by fixed number of iterations.

The top pull widths (Fig. 5.11) have constant offset from expected value, except the case of absolute stopping condition (blue color), which has slight slope with respect to corresponding generated asymmetry of pseudo-experiment.Generally, we can say that the uncertainties are over estimated with higher number of iterations for top pseudo-experiments.

For lepton case (Fig. 5.12) the uncertainties are consistent with slight fluctuations.

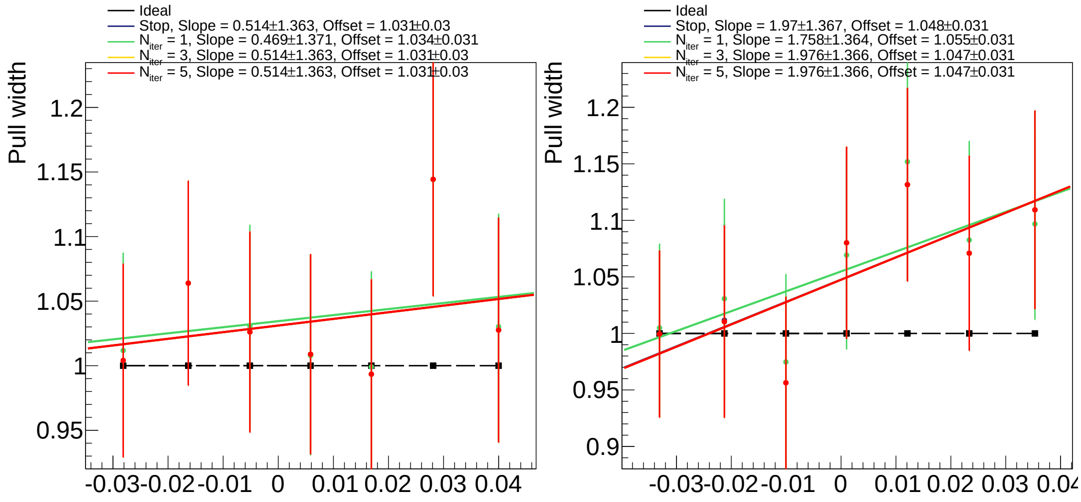

(a) All channels together.

(b) *ee* channel.

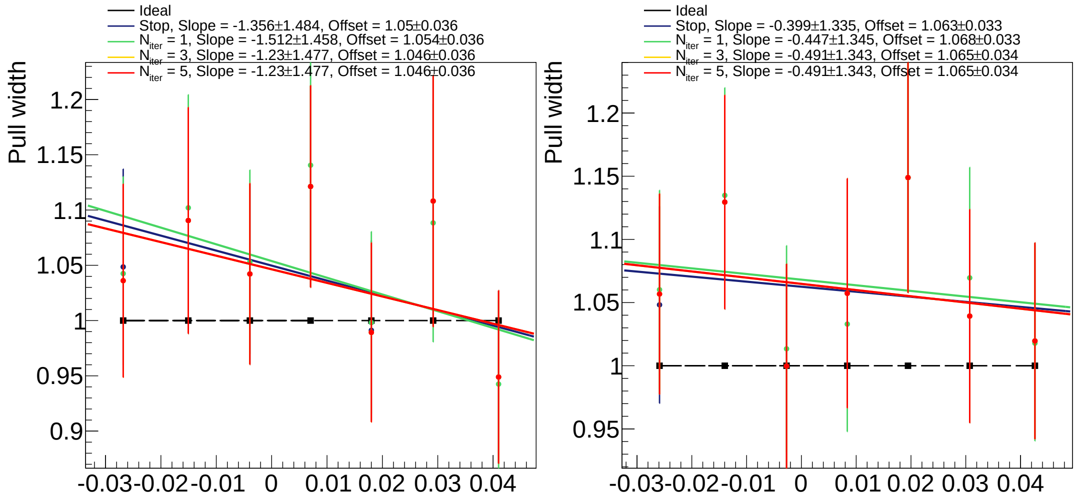

(c) $e\mu$ channel.

(d) $\mu\mu$ channel.

Figure 5.12: Lepton pull width with respect to generated asymmetry (channel per sub-figure). The dark blue colour represents number of iterations needed to fulfil the absolute stopping condition. Other colours are unfolded by fixed number of iterations.

5.4 Corrections and uncertainties

As has been showed above for top pseudo-experiments we can find the number of iterations, which provides unfolded asymmetry consistent with true value at the level of $\sim 1\sigma$. However for lepton pseudo-experiments, there is significant bias, which is constant with respect to number of iterations. Therefore it is needed to provide corrections of the asymmetry value.

We have found linear dependence of mean unfolded asymmetry in pseudo-experiments $< A_{\mathrm{C}}^{\mathrm{unf}} >$ with respect to the generated asymmetry $A_{\mathrm{C}}^{\mathrm{Gene}}$. If we define corrected asymmetry $A_{\mathrm{C}}^{\mathrm{corr}}$ as in Eq. 5.18b and we expect Gaussian distribution, the mean corrected asymmetry in pseudo-experiments $< A_{\mathrm{C}}^{\mathrm{corr}} >$ should be equal to generated asymmetry Eq. 5.18.

$$< A_{\mathrm{C}}^{\mathrm{unf}} > = a_1 \cdot A_{\mathrm{C}}^{\mathrm{Gene}} + b_1 \tag{5.18a}$$

$$A_{\mathrm{C}}^{\mathrm{corr}} \equiv \frac{A_{\mathrm{C}}^{\mathrm{unf}} - b_1}{a_1} \tag{5.18b}$$

$$< A_{\mathrm{C}}^{\mathrm{corr}} > = A_{\mathrm{C}}^{\mathrm{Gene}} \tag{5.18c}$$

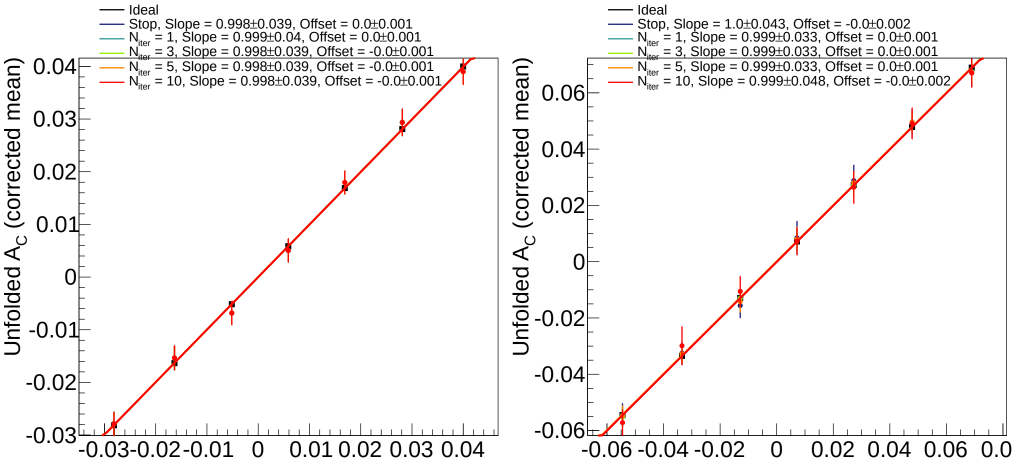

(a) Lepton pseudoexperiments.

(b) Top pseudoexperiments.

Figure 5.13: Unfolded asymmetry after correction w.r.t. generated asymmetry (all channels together). The dark blue colour represents number of iterations needed to fulfil the absolute stopping condition. Other colours are fixed-iterations unfolded. For more description see text.

The pseudo-experiments has been performed again and correction described above Eq. 5.18b has been applied. On Fig. 5.13 are plotted mean values of corrected unfolded asymmetry. As the Fig. 5.13 shows all lines are overlapped, it means the bias has been suppressed as has been expected.

As has been written above, if pull width is equal to one then the estimation of uncertainty is consistent to statistical observation in PE. We found linear dependence of pull width with respect to generated asymmetry (see Fig. 5.11). The fit of pull width was performed on pull distribution after correction of mean value and from fitted parameters the correction has been applied.

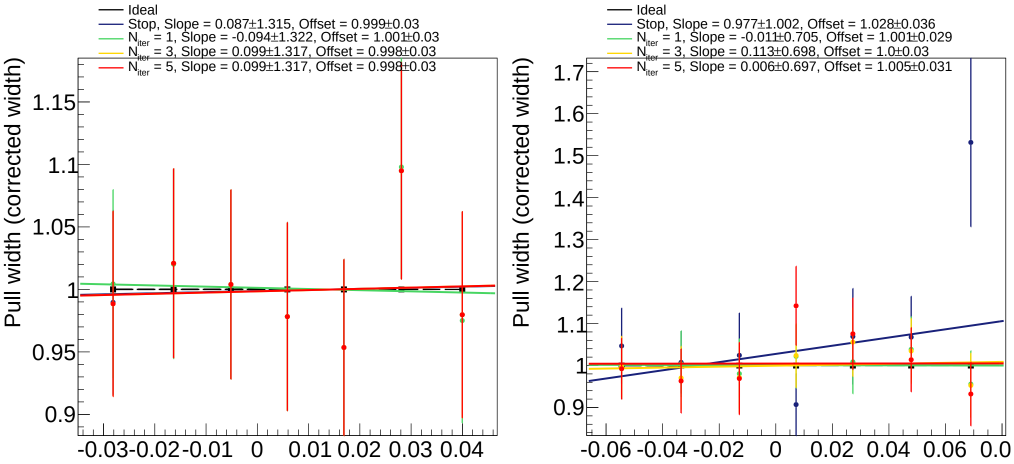

(a) Lepton pseudoexperiments.

(b) Top pseudoexperiments.

Figure 5.14: Pull width asymmetry after corrections w.r.t. generated asymmetry (all channels together). The dark blue colour represents number of iterations needed to fulfil the absolute stopping condition. Other colours are fixed-iterations unfolded. For more description see text.

The final corrected pull width is consistent with one for all fixed iteration lines, as it is shown on Fig. 5.14. The line corresponding to iteration-stopping condition has slope and therefore it will be better to find right number of iterations needed for data and then apply correction from fixed iteration pseudo-experiments.

The figures in this section has been produced from all channels together.

Conclusions

In this work, the charge asymmetry in $t\bar{t}$ production in dilepton channel has been studied.

The main goal of this thesis has been the unfolding of $\Delta|y_{t\bar{t}}|$ and $\Delta|\eta_{\ell^+\ell^-}|$ distributions from detector to parton level. The Bayesian iterative method has been chosen for deconvolution. The two parameters has been optimalized: number of bins of the unfolded distribution and number of iterations. The unfolding of the distribution with many bins appears to be inappropriate. The final number of bins has been estimated to be eight.

For the second parameter, number of iterations, we propose the condition, when to stop the procedure. This has been studied in the pseudo-experiments, which show we get unbiased result within uncertainties for $\Delta|y_{t\bar{t}}|$ distribution. The number of iteration needed to obtain unbiased result is somwhere 5 to 10 iterations. For the $\Delta|\eta_{\ell^+\ell^-}|$ distribution it was necessary to apply the corrections.

To meet the above goal, it was needed to master few basic steps. Firstly, it was needed to get acquainted with the software of ATLAS collaboration. Secondly, it was necessary to learn about the $t\bar{t}$ event selection and reconstruction. Finally, it was necessary to study the existing methods of unfolding.

As next step is needed to apply the method to data and estimate related systematic uncertainties. In the future, it is desirable to perform the unfolding in two dimensions as function of some kinematic characteristics like invariant mass or transverse momentum of $t\bar{t}$ system, since the charge asymmetry is predicted to be a function of such parameters. Moreover, one can think also about the unfolding to particle rather to parton level to minimize the dependence on Monte-Carlo generators.

APPENDIX A

RESPONSE MATRICES

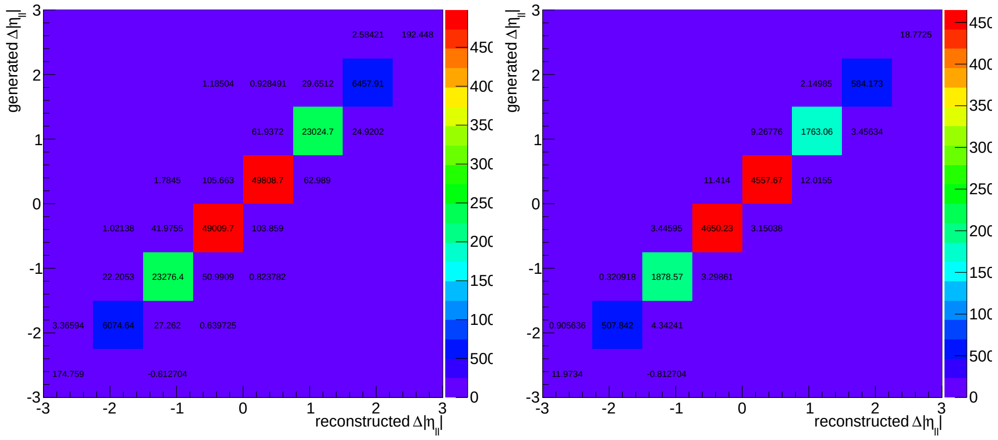

(a) All channels together.

(b) ee channel.

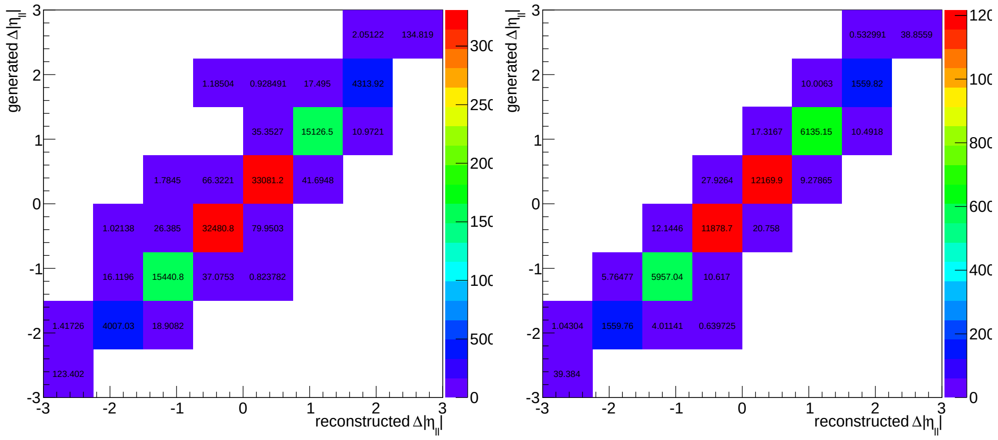

(c) $e\mu$ channel.

(d) $\mu\mu$ channel.

Figure A.1: Lepton response matrices per channel, showed as 2-dimensional histograms. The distribution represent number of events in generated vs. reconstructed $\Delta|\eta_{\ell^+\ell^-}|$ distributions.

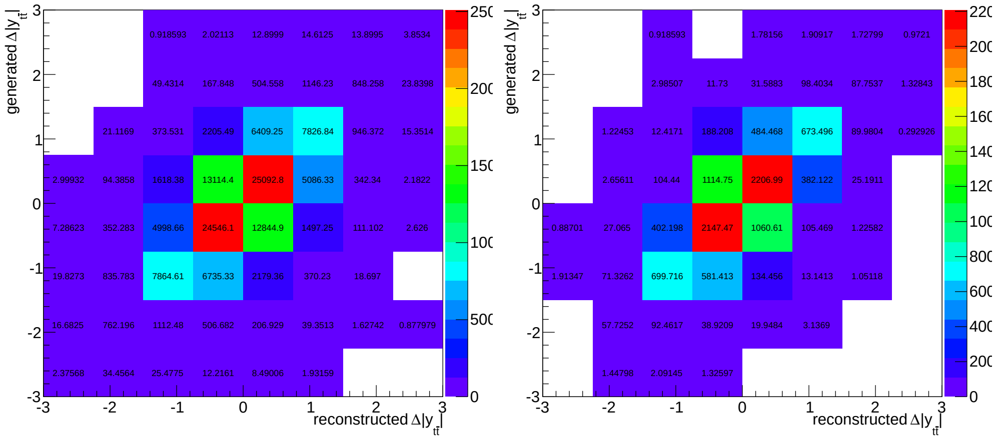

(a) All channels together.

(b) *ee* channel.

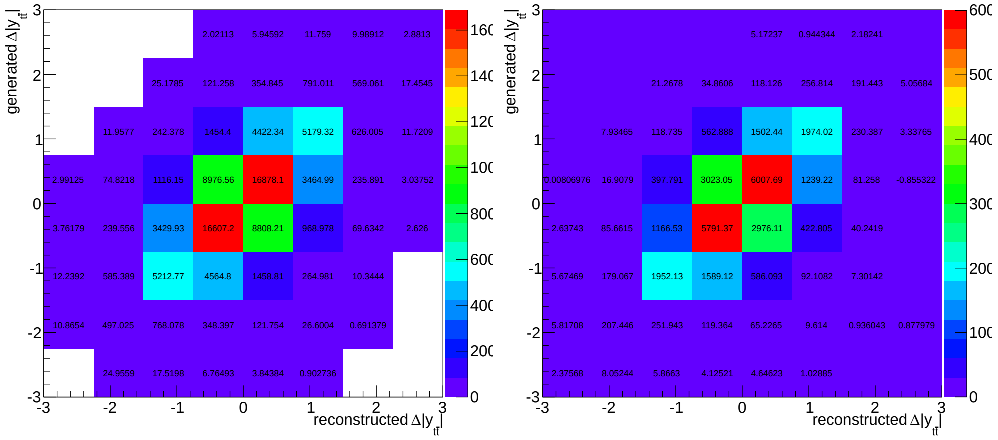

(c) $e\mu$ channel.

(d) $\mu\mu$ channel.

Figure A.2: Top response matrices per channel, showed as 2-dimensional histograms. The distribution represent number of events in generated vs. reconstructed $\Delta|y_{t\bar{t}}|$ distributions.

Bibliography

[1] C. Burgess and G. Moore. *The Standard Model: A Primer.* Cambridge University Press, 2012.

[2] I. Stoll. *Dejiny fyziky.* Prometheus, 2009.

[3] W. Pauli. Über den Zusammenhang des Abschlusses der Elektronengruppen im Atom mit der Komplexstruktur der Spektren. *Zeitschrift für Physik*, 31(1):765–783, 1925.

[4] Particle Data Group. Review of Particle Physics. *Phys. Rev. D*, 86(1):010001, Jul 2012.

[5] W. Heisenberg. Über den anschaulichen Inhalt der quantentheoretischen Kinematik und Mechanik. *Zeitschrift für Physik*, 43:172–198, 1927.

[6] L. Landau and E.M. Lifshitz. Mechanics, Third Edition: Volume 1 (Course of Theoretical Physics) . 1976.

[7] E. Noether. Invariant variation problems. *Transport Theory and Statistical Physics*, 1:186–207, 1971. M. A. Tavel's English translation of Noether's Theorems (1918), reproduced by Frank Y. Wang.

[8] M. Aivazis. *Group Theory in Physics: Problems and Solutions.* World Scientific Publishing Company, 1991.

[9] F. Abe et al. Evidence for top quark production in $\bar{p}p$ collisions at \$sqrts= $1.8TeV$. *Phys. Rev. Lett.*, 73(2):225–231, 1994.

[10] S. Abachi et al. Search for the top quark in $p\bar{p}$ collisions at $\sqrt{s}$ =1.8 TeV. *Phys. Rev. Lett.*, 72:2138–2142, 1994.

[11] M. Aliev. – HATHOR – HAdronic Top and Heavy quarks crOss section calculatoR . *Comput.Phys.Commun.*, 182:1034–1046, 2011.

[12] The ATLAS Collaboration. Searches for Single Top-Quark Production with the ATLAS Detector in pp Collisions at $\sqrt{(}s) = 7\,TeV$. 2011.

[13] G. Kane and Pierce A. Perspectives on LHC Physics. 2008.

[14] O. Antunano, J. H. Kuhn, and G. Rodrigo. Top Quarks, Axigluons and Charge Asymmetries at Hadron Colliders . *Phys.Rev.*, D77:014003, 2008.

[15] The CDF Collaboration. Measurement of the top quark forward-backward production asymmetry and its dependence on event kinematic properties. *Phys. Rev. D*, 2012.

[16] The CDF Collaboration. Evidence for a Mass Dependent Forward-Backward Asymmetry in Top Quark Pair Production. *Phys.Rev.*, D83:112003, 2011.

[17] The D0 Collaboration. Forward-backward asymmetry in top quark-antiquark production. *Phys.Rev.*, D84:112005, 2011.

[18] The ATLAS Collaboration. Measurement of the charge asymmetry in top quark pair production in pp collisions at sqrt(s) = 7 TeV using the ATLAS detector. *Eur.Phys.J.*, C72:2039, 2012.

[19] The ATLAS Collaboration. The ATLAS Experiment at the CERN Large Hadron Collider. *Journal of Instrumentation*, 3(08):S08003, 2008.

[20] D. Green. At the Leading Edge: The ATLAS and CMS LHC Experiments. 2011.

[21] CERN Web Communications. The name CERN. `http://public.web.cern.ch/public/en/About/Name-en.html`, 2008.

[22] Ch. Lefèvre. The CERN accelerator complex. `http://cds.cern.ch/record/1260465`, 2008.

[23] CERN Communication Group. CERN FAQ – LHC the guide. `http://cdsweb.cern.ch/record/1165534/files/CERN-Brochure-2009-003-Eng.pdf`, 2009.

[24] J. Pequenao. Computer generated image of the whole ATLAS detector. 2008.

[25] A. Artamonov et al. The ATLAS Forward Calorimeter . *Journal of Instrumentation*, 3(02):P02010, 2008.

[26] G. Avolioa, S. Ballestrerob, and W. Vandellic. ATLAS TDAQ system: current status and performance . 2012.

[27] The ATLAS Collaboration. ATLAS Computing Technical Design Report . 2005.

[28] The ATLAS Collaboration. ATLAS Fact Sheet. http://www.atlas.ch/pdf/atlas_factsheet_all.pdf, 2012.

[29] G. Barrand et al. GAUDI - A Software Architecture and Framework for building HEP Data Processing Applications . 2001.

[30] The Apache Software Foundation. Apache™ Subversion®. http://subversion.apache.org/, Dec 2012.

[31] Ch. Arnault. Configuration Management Tool . http://www.cmtsite.org/, Dec 2012.

[32] S. Spangolo et al. The Description of the Atlas Detector. In *Computing in High Energy Physics and Nuclear Physics* , 2004.

[33] P. J. Clark. The ATLAS Detector Simulation . 2011.

[34] G. Cowan. *Statistical Data Analysis* . 1998.

[35] Z. Marshall. The ATLAS Simulation Software . 2009.

[36] I. Ueda. The Present and Future Challenges of Distributed Computing in the ATLAS experiment. Technical Report ATL-SOFT-PROC-2012-069, CERN, Geneva, Nov 2012.

[37] T. Maeno and ... Evolution of the ATLAS PanDA Production and Distributed Analysis System . 2012.

[38] R. Brun and F. Rademakers. ROOT - An Object Oriented Data Analysis Framework. Nucl. Inst. & Meth. in Phys. Res.(A 389):81–86, 1997.

[39] The ROOT Team. ROOT - A Data Analysis Framework. `http://root.cern.ch/drupal/`, Dec 2012.

[40] The Latex project team. LaTeX – A document preparation system. `http://www.latex-project.org/`, 2012.

[41] D. Berge et al. SFrame - A ROOT data analysis framework . `http://sourceforge.net/projects/sframe/`, Dec. 2012.

[42] N. Krumnack. RootCore. 2012.

[43] The Kitware team. CMake – Cross platform make. `http://www.cmake.org/`, Dec. 2012.

[44] Inc. Free Software Foundation. The GNU Make Manual. `http://www.gnu.org/software/make/manual/make.html`, 2012.

[45] R. Lysák. TopDilAna - package for dilepton mini-ntuple production. `svn+ssh://svn.cern.ch/reps/atlasinst/Institutes/Kosice/DiLepton/packages/TopDilAna/tags/TopDilAna-00-00-03`, 2012.

[46] W. H. Press, S. A. Teukolsky, W. T. Vetterling, and B. P. Flannery. *Numerical Recipes 3rd Edition: The Art of Scientific Computing.* Cambridge University Press, New York, NY, USA, 3 edition, 2007.

[47] The ATLAS Collaboration. Measurement of the charge asymmetry in dileptonic decay of top quark pairs in pp collisions at $\sqrt{s} = 7$ TeV using the ATLAS detector. Technical Report ATLAS-CONF-2012-057, CERN, 2012.

[48] The ATLAS Collaboration. Electron performance measurements with the ATLAS detector using the 2010 LHC proton-proton collision datavidence for a Mass Dependent Forward-Backward Asymmetry in Top Quark Pair Production. *Eur.Phys.J.*, C72:1909, 2012.

[49] M. Cacciari, G. P. Salam, and G. Soyez. The Anti-k(t) jet clustering algorithm. *JHEP*, 0804:063, 2008.

[50] The ATLAS Collaboration. Jet energy measurement with the ATLAS detector in proton-proton collisions at $\sqrt{s} = 7$ TeV. *Eur.Phys.J.*, C, 2011.

[51] S. Frixione and B. R. Webber. Matching NLO QCD Computations and Parton Shower Simulations. 2002.

[52] Particle Data Group. Review of Particle Physics. *J.Phys.*, G37:075021, 2010.

[53] L. Hung-Liang et al. New parton distributions for collider physics. *Phys.Rev.*, D82:074024, 2010.

[54] The ATLAS Collaboration. New ATLAS event generator tunes to 2010 data. Technical report, CERN, 2011.

[55] G. Corcella et al. HERWIG 6: An Event generator for hadron emission reactions with interfering gluons (including supersymmetric processes). *JHEP*, 0101:010, 2001.

[56] J.M. Butterworth. Multiparton interactions in photoproduction at HERA. *Z.Phys*, C72:637–646, 1996.

[57] B.P. Kersevan and E. Richter-Was. The Monte Carlo event generator AcerMC version 2.0 with interfaces to PYTHIA 6.2 and HERWIG 6.5. *TPJU*, 6, 2004.

[58] M. L. Mangano et al. ALPGEN, a generator for hard multiparton processes in hadronic collisions. *JHEP*, 0307:001, 2003.

[59] G. Cowan. A survey of unfolding methods for particle physics. *Conf.Proc.*, C0203181:248–257, 2002.

[60] J. Cúth. TopDilUnf - package for unfolding top charge asymmetry in dilepton channel. http://svn.cern.ch/guest/jcuth/dev/TopDilUnf/tags/TopDilUnf-00-00-01/, Dec 2012.

[61] G. D'Agostini. A multidimensional unfolding method based on Bayes' theorem . 1994.

[62] R. Barlow. Resampling and Bootstrap. *SLUO Lectures on Statistics and Numerical Methods in HEP*, Lecture 6, 2000.